Very large release of mostly volcanic carbon during the Paleocene-Eocene Thermal Maximum

Marcus Gutjahr[1,2*], Andy Ridgwell[3,4], Philip F. Sexton[5], Eleni Anagnostou[1], Paul N. Pearson[6], Heiko Pälike[7], Richard D. Norris[8], Ellen Thomas[9,10] and Gavin L. Foster[1]

[1] Ocean and Earth Science, National Oceanography Centre Southampton, University of Southampton, UK

[2] GEOMAR Helmholtz Centre for Ocean Research Kiel, Germany mgutjahr@geomar.de

(* corresponding author)

[3] School of Geographical Sciences, Bristol University, Bristol, UK

[4] Department of Earth Sciences, University of California-Riverside, Riverside, CA, USA

[5] School of Environment, Earth & Ecosystem Sciences, The Open University, Milton Keynes, UK

[6] School of Earth and Ocean Sciences, Cardiff University, Cardiff, UK

[7] MARUM, Center for Marine Environmental Sciences, University of Bremen, Germany

[8] Scripps Institution of Oceanography, University of California, San Diego, La Jolla, U.S.A.

[9] Department of Geology and Geophysics, Yale University, New Haven CT, U.S.A.

[10] Department of Earth and Environmental sciences, Wesleyan University, Middletown CT, USA

Global warming during the Palaeocene-Eocene Thermal Maximum[1,2] (PETM, ~56 Ma) is commonly interpreted as being primarily driven by the destabilization of carbon from surficial sedimentary reservoirs such as methane hydrates[3]. However, the source(s) of carbon remain controversial[1,3-5]. Resolving this is key to understanding the proximal cause, as well as quantifying the roles of triggers versus feedbacks in driving the event. Here we present new boron isotope data – a proxy for seawater pH – that demonstrate the occurrence of persistently suppressed surface ocean pH across the PETM. Our pH data, alongside a paired carbon isotope record, are assimilated in an Earth system model to reconstruct the unfolding carbon cycle dynamics across the event[6,7]. We find strong evidence for a much larger (>10,000 PgC) and on average isotopically heavier carbon source than considered previously[8,9]. This leads us to identify volcanism associated with the North Atlantic Igneous Province, rather than carbon from a surficial reservoir, as the main driver of the PETM[10,11]. We also find that, although amplifying organic carbon feedbacks with climate likely played only a subordinate role in driving the event, enhanced organic matter burial was important in ultimately sequestering the released carbon and accelerating the recovery of the Earth system[12].

Aside from climate[13] and ecological sensitivities[14], arguably the greatest uncertainties surrounding the response of the Earth system to massive carbon release concern the role of carbon-cycle feedbacks[15]. A past event with considerable potential to evaluate such feedbacks is the Palaeocene-Eocene Thermal Maximum (PETM)[1] – a 4-5°C transient surface warming[2] associated with ecological disruption occurring around 55.8 million years ago[16]. Estimates of total carbon release vary from ~3,000 PgC to over 10,000 PgC[7,8], spanning the range of present-day fossil fuel reserves[17] but equally reflecting considerable uncertainty in current understanding. The source(s) of carbon is also highly uncertain, and has been proposed to involve methane hydrates[3], permafrost[4] and marine sedimentary[5] organic matter. To further complicate the matter, proposed triggers for the PETM include orbital variations[4] and an extraterrestrial impact[18]. Massive flood basalts and sill emplacement occurring around the time of the PETM and associated with the North Atlantic Igneous Province (NAIP)[10,11,19], constitute an additional potential source of carbon, but one not linked to a feedback with climate. If we are to fully understand the paleo-record, as well as exploit it to improve our understanding of the longer-term consequences of anthropogenic carbon emissions, we must resolve the balance of carbon source(s) that gave rise to the PETM, and thereby deconvolve the role(s) of triggers versus feedbacks. To provide new insight into the amount and source of

carbon involved in PETM warming, we present new, paired, surface ocean boron (a well-established proxy for ambient surface seawater pH[20,21]) and carbon isotope data, and simultaneously use these to constrain the time-varying sources and sinks of carbon across the PETM in a novel data assimilation approach in an Earth System model (ESM).

We generated near-continuous boron, oxygen and carbon isotope records from NE Atlantic DSDP Site 401, using the surface ocean mixed-layer dwelling foraminifer *Morozovella subbotinae* (Fig. 1). We sampled the sediment sequence over an interval corresponding to ~300 ka preceding the carbon isotope excursion (CIE) to ~500 ka afterwards, using a new stratigraphy for Site 401 (Methods). To avoid alignment issues between proxies, we measured boron, oxygen and carbon isotopic compositions on the same samples (Figs. 1a, c, e and Extended Data Fig. 2).

Our measured CIE magnitude at Site 401 of -3.4‰ (Fig. 1a) is at the upper end of planktic foraminiferal $\delta^{13}C$ records (minimum CIE: -0.7, maximum -4.4, average -2.7, n=36)[1], suggesting that our sampling encompasses close to the full magnitude of the CIE (see Methods). The CIE is accompanied by a decrease in $\delta^{11}B$ of almost 1.7‰ (Fig. 1c). The lowest $\delta^{13}C$ and $\delta^{11}B$ values are both observed about ~25 ka after the onset of the CIE in our preferred age model, giving an inferred duration of the onset phase of the CIE in good agreement with an independently dated record from Spitsbergen[16].

Because of uncertainties in early Cenozoic seawater boron isotopic composition ($\delta^{11}B_{SW}$), we tie our initial, pre-CIE boron isotope derived pH to mean ocean pH (7.75) as simulated by the 'GENIE' Earth System Model (ESM)[6] and following the approach of a previous PETM model-data pH study[20]. Our $\delta^{11}B$ measurements then dictate the timing and magnitude of how ocean pH deviated from this value across the PETM. In our pH reconstruction, we calculate an uncertainty envelope accounting for uncertainties in surface ocean temperature and salinity plus $\delta^{11}B$ measurement errors, and test two contrasting end-member $\delta^{11}B$-pH calibrations for the extinct foraminifer *M. subbotinae* (see Methods). We focus on the $\delta^{11}B_{foram} = \delta^{11}B_{borate}$ calibration, giving an estimated $\delta^{11}B_{SW}$ (38.9 ± 0.4‰) consistent with a recent reconstruction of Eocene $\delta^{11}B_{SW}$ based on $\delta^{11}B$[21].

Evolution of ocean pH across the PETM is characterized by a negative excursion of 0.27 (range: 0.18-0.41) or 0.36 (0.21-0.56) pH units, depending on which $\delta^{11}B$-pH calibration is used (Fig. 2 and Extended Data Fig. 3a), and in general agreement with a recently published PETM $\delta^{11}B$ record[20] (Fig. 2). The wide geographic distribution, but close

correspondence in magnitude of all PETM δ^{11}B-pH records (Pacific, S. Atlantic and N. Atlantic) gives us confidence that a global surface pH excursion signal is captured at DSDP Site 401. The fact that ocean surface pH responds relatively uniformly in models[14] supports the evidence from multiple δ^{11}B records (Fig. 2) that a single open ocean site can be representative of the global trend (see Methods).

To reconstruct PETM carbon release and its average isotopic composition, we devised a novel data assimilation methodology. We build on previous work[7] in which a single δ^{13}C record was assimilated ('inverted') to constrain the time-varying addition of carbon, but here exploit a more direct indicator of carbon addition – ocean surface pH (Fig. 2). This allows our δ^{13}C record to simultaneously provide a second, independent constraint on the isotopic composition of the carbon emissions in a transient, 500 kyr duration assimilation of both records (see Methods). We explored a wide range of different model parameterizations and proxy assumptions (Extended Data Table 1a) but focus here on the results of the data assimilation of the smoothed record.

With our preferred age model ('R07sm', Extended Data Table 1a) we diagnose a cumulative PETM carbon release reaching ~10,200 PgC with almost all emissions occurring in the first 50 kyr (Fig. 3d). This estimate is largely independent of the choice of age model (Extended Data Table 1), which primarily affects the cumulative carbon emissions associated with the onset interval itself (defined as: from the first trace of the δ^{13}C decline in our records up to peak CIE values) rather than with total emissions associated with the event as a whole. We demonstrate this in idealized model experiments (Extended Data Fig. 5 and Extended Data Table 1b) in which we find total carbon emissions over 50 kyr essentially independent of the assumed duration of the onset interval, and varying by only ±20% at the 20 kyr horizon (Extended Data Fig. 5 and Extended Data Table 1b). Thus, it is the extended duration of low pH across the PETM as a whole and the existence of the so-called carbon isotope 'plateau'[2], rather than the duration of the onset interval alone, that lead to our diagnosis of total PETM emissions on the order of 10,000 PgC. Uncertainty in the duration of low pH equates to ~100 PgC kyr^{-1} at the 50 kyr horizon (Extended Data Fig. 5), consistent with the ~12,000 PgC total emissions deduced for our alternative age model with an extended duration of low pH (Extended Data Fig. 3c).

In response to carbon emissions, atmospheric pCO_2 in the model increases from ~866 to a peak PETM value of 2176 +1904/-669 μatm, consistent with independent atmospheric pCO_2 constraints based on variable terrestrial and marine δ^{13}C gradients over the PETM[22]. The

corresponding projected annual mean sea surface temperature (SST) increase is 3.6°C – close to the observation-based global mean warming estimate of 4-5°C[2]. Also in response to carbon emissions (and surface ocean pH suppression), there is a shoaling of the carbonate compensation depth (CCD) in the model – the depth horizon below which calcium carbonate ($CaCO_3$) is not preserved[23] (Extended Data Fig. 7). In previous global carbon cycle model analyses of the PETM, the CCD has been used as a data constraint, with the conclusion that carbon emissions on the order of 10,000 PgC are too high[8]. In contrast, here, the relatively long (>50 kyr) duration of low ocean pH conditions (Fig. 3) in conjunction with weathering feedbacks, leads to a partial decoupling of pH and ocean carbonate saturation[24], hence a relatively muted response of the CCD despite the large emissions (Extended Data Fig. 7 and Methods).

Diagnosed carbon emission rates peak at 0.58 PgC yr^{-1} (Fig. 3c; Extended Data Table 1a), although we assign rather less confidence to these, because their value is sensitive to the duration of the onset of the PETM and hence the specific age model (Extended Data Table 1a). To put this in perspective, for carbon input rates to approach those of current fossil fuel emissions (~10 PgC yr^{-1} [17]), the PETM onset would have to occur within 200-500 yr – a duration not supported by any independent age model[7,16,24,25]. The much lower than modern carbon emissions rate we diagnose here then implies reduced PETM ocean acidification impacts (especially in carbonate saturation) compared to the future[6,15]. However, we cannot rule out multiple, short-lived pulses of carbon release >0.58 PgC yr^{-1} having occurred throughout an extended (e.g. 20 kyr) onset[24].

In addition to the emissions diagnosed by matching the pH decline, using the $\delta^{13}C$ data as an independent constraint leads us to deduce a flux-weighted mean $\delta^{13}C$ of released carbon of -11‰ (Fig. 3f, n). However, the smoothed $\delta^{13}C$ record (-2.6‰ excursion) on which we focus, very likely underestimates the isotopic magnitude of the event. For instance, if the 'true' PETM CIE was as large as -4.0‰[7,24] and we simply proportionally scale $\delta^{13}C_{input}$, diagnosed on the basis of a -2.6‰ excursion, we obtain a more depleted mean source of -17‰. Uncertainty in our ocean pH reconstruction also affects the diagnosed carbon source composition. Our minimum pH decrease of 0.18 pH units requires only 5,700 PgC, with a mean $\delta^{13}C_{input}$ of -19‰. However, the comparatively muted surface warming seen in this 'minimal pH change' model experiment (2.25°C, Extended Data Table 1a – experiment 'R07am_HI') is difficult to reconcile with an observed warming of 4-5°C[2]. Conversely, the upper end of our measured pH increase would require emission of considerably more carbon

147 (19,960 PgC) with a correspondingly heavier carbon isotopic composition of -6.6‰
148 (Extended Data Table 1a).

149 Our diagnosed carbon input over the event likely reflects a combination of carbon
150 source(s) – for instance, a mean of -11‰ could reflect a 75% contribution of mantle-derived
151 carbon ($\delta^{13}C_{source}$ ~-6‰) plus 25% from permafrost (~-26‰), or 90% mantle-derived plus
152 10% methane hydrates (~-60‰). In such scenarios, volcanism triggered the PETM, and
153 thawing permafrost in Antarctica[4] or destabilization of methane hydrates provided amplifying
154 feedback. Assuming a -4‰ magnitude excursion and mean $\delta^{13}C_{input}$ of -17‰ still requires a
155 substantial CO_2 contribution from volcanism[10], but would allow for the possibility of a greater
156 role for organic carbon feedbacks – almost 60% for organic matter or ~20% for methane
157 hydrates.

158 To date, the PETM has predominantly been viewed as an event dominated by feedbacks
159 between climate and reservoirs of carbon[3]. Yet, there is abundant evidence of an intimate link
160 in time with the opening of the North Atlantic[11], with volcanism and ash deposition occurring
161 from immediately prior to PETM onset, as also recorded by declining $^{187}Os/^{188}Os$ in
162 sediments[19]. Radiometric dating places the PETM coincident with a ~1 Myr interval of
163 massive flood basalt volcanism[11] and the emplacement of magmatic sills[26], both of which
164 represent large carbon sources. Degassing CO_2 from magma yields an estimated 3,600-6,000
165 gC m^{-3} [27] and combining this with the estimated volume of the NAIP as a whole (5×10^6 km^3
166 to 10×10^6 km^3 [11,27]), equates to a potential carbon source of 18,000-60,000 PgC. The
167 interaction of magmatism with organic rich sediments could enhance carbon release via
168 thermogenic methane production[10,11], which is estimated to range from 3,000-6,000 PgC[28] to
169 as high as 15,000 PgC[10]. Available carbon reservoirs are thus more than sufficient to provide
170 the 10,200-12,200 PgC required by our data assimilation and we further note that an all-
171 volcanic carbon driver scenario for the PETM is possible if thermogenic methane[10,11]
172 provided the isotopically lighter end-member. On the other hand, NAIP magmatic activity
173 took place over several million years[10,11] and how carbon emissions were distributed with
174 time over this interval is currently unknown. Dating, biostratigraphy, and seismic constraints
175 do however: (1) place an interval of volcanism in East Greenland[11] and sill emplacement in
176 the Vøring Basin (offshore Norway)[26], both coeval with PETM onset, (2) identify 100s of
177 degassing structures consistent with thermogenic carbon release as forming close to the P-E
178 boundary[10] and with one structure constrained to have been active during the body of the
179 PETM itself[9]. Release of a disproportionate amount of NAIP carbon associated with the

PETM is hence consistent with available geological evidence as well as our data-inferred carbon source and total release. More work dating further specific volcanic episodes and refining carbon reservoir estimates is however clearly needed.

Our paired $\delta^{11}B$-$\delta^{13}C$ data also provide insights into climate system recovery from PETM warming. Once carbon emissions ceased (ca. ~55 kyr after PETM initiation – Fig. 3c), elevated global temperatures (Fig. 3a) and enhanced rates of silicate weathering (Fig. 3c) in cGENIE (see Methods) drive a trend of increasing ocean surface pH that closely follows the observed surface ocean pH recovery (Fig. 3b). However, we find a model-data misfit of up to ~1‰ in $\delta^{13}C$ during the recovery phase (Fig. 3e). We therefore performed an additional set of experiments in which, after peak CIE, organic carbon (C_{org}) is removed from the ocean surface[29] and assumed buried whenever modelled mean ocean surface $\delta^{13}C$ registered lower values than the observed trend (see Methods). These final experiments provide close agreement with the recovery trend in the $\delta^{13}C$ data (Fig. 3m), with cumulative C_{org} burial (Fig. 3l, blue bars) of 2,500 PgC (at an average modelled marine value of -30.5‰), in agreement with other estimates (~2,000 PgC)[12] of the role of enhanced organic matter burial in PETM recovery[29] as well as the ensuing reduction in deep-sea oxygenation[30].

These findings collectively lead us to a view of the PETM as having been on the smaller end of a spectrum of severe perturbations of climate and carbon cycling during the Cretaceous and Jurassic (Ocean Anoxic Events – OAEs[30,31]), despite it having been by far the largest end-member in a series of Paleocene-Eocene 'hyperthermal' events[32]. Our pH reconstruction, in conjunction with the observed $\delta^{13}C$ decline, constrains the dominant carbon source during the PETM onset to have had a comparatively heavy carbon isotope ratio, strongly implicating volcanism as having been dominant in triggering and driving the event. Our inferred mean $\delta^{13}C$ source of -11 to -17‰ is consistent with the isotopically relatively heavy source (ca. -15‰[33]) inferred for the end-Permian event, suggesting mechanistic similarities between the two events[27]. The implied important role for organic carbon deposition in the recovery from peak warming[12] represents another diagnostic feature of OAEs[31] (and end-Permian). Further quantifying and understanding the precise role of feedbacks – both those amplifying initial CO_2 release, and those aiding recovery from global warming – is arguably where the PETM is of greatest value in helping reduce uncertainties surrounding the response of the global carbon cycle and climate system to perturbation.

1 McInerney, F. A. & Wing, S. L. The Paleocene-Eocene Thermal Maximum: A perturbation of carbon cycle, climate, and biosphere with implications for the future. *Annual Review of Earth and Planetary Sciences* **39**, 489-516 (2011).

2 Dunkley Jones, T. *et al.* Climate model and proxy data constraints on ocean warming across the Paleocene-Eocene Thermal Maximum. *Earth-Science Reviews* **125**, 123-145 (2013).

3 Dickens, G. R., O'Neil, J. R., Rea, D. K. & Owen, R. M. Dissociation of oceanic methane hydrate as a cause of the carbon isotope excursion at the end of the Paleocene. *Paleoceanography* **10**, 965-971 (1995).

4 DeConto, R. M. *et al.* Past extreme warming events linked to massive carbon release from thawing permafrost. *Nature* **484**, 87-91 (2012).

5 Higgins, J. A. & Schrag, D. P. Beyond methane: Towards a theory for the Paleocene-Eocene Thermal Maximum. *Earth and Planetary Science Letters* **245**, 523-537 (2006).

6 Ridgwell, A. & Schmidt, D. N. Past constraints on the vulnerability of marine calcifiers to massive carbon dioxide release. *Nature Geoscience* **3**, 196-200 (2010).

7 Cui, Y. *et al.* Slow release of fossil carbon during the Palaeocene-Eocene Thermal Maximum. *Nature Geoscience* **4**, 481-485 (2011).

8 Zeebe, R. E., Zachos, J. C. & Dickens, G. R. Carbon dioxide forcing alone insufficient to explain Palaeocene-Eocene Thermal Maximum warming. *Nature Geoscience* **2**, 576-580 (2009).

9 Frieling, J. *et al.* Thermogenic methane release as a cause for the long duration of the PETM. *Proceedings of the National Academy of Sciences* **113**, 12059-12064 (2016).

10 Svensen, H. *et al.* Release of methane from a volcanic basin as a mechanism for initial Eocene global warming. *Nature* **429**, 542-545 (2004).

11 Storey, M., Duncan, R. A. & Swisher, C. C. Paleocene-Eocene Thermal Maximum and the Opening of the Northeast Atlantic. *Science* **316**, 587-589 (2007).

12 Bowen, G. J. & Zachos, J. C. Rapid carbon sequestration at the termination of the Palaeocene-Eocene Thermal Maximum. *Nature Geoscience* **3**, 866-869 (2010).

13 Rohling, E. J. *et al.* Making sense of palaeoclimate sensitivity. *Nature* **491**, 683-691 (2012).

14 Gibbs, S. J. *et al.* Ocean warming, not acidification, controlled coccolithophore response during past greenhouse climate change. *Geology* **44**, 59-62 (2016).

15 Hönisch, B. *et al.* The geological record of ocean acidification. *Science* **335**, 1058-1063 (2012).

16 Charles, A. J. *et al.* Constraints on the numerical age of the Paleocene-Eocene boundary. *Geochemistry Geophysics Geosystems* **12**, Art. No. Q0AA17 (2011).

17 Le Quéré, C. *et al.* Global Carbon Budget 2016. *Earth Syst. Sci. Data* **8**, 605-649 (2016).

18 Schaller, M. F., Fung, M. K., Wright, J. D., Katz, M. E. & Kent, D. V. Impact ejecta at the Paleocene-Eocene boundary. *Science* **354**, 225 (2016).

19 Wieczorek, R., Fantle, M. S., Kump, L. R. & Ravizza, G. Geochemical evidence for volcanic activity prior to and enhanced terrestrial weathering during the Paleocene Eocene Thermal Maximum. *Geochimica et Cosmochimica Acta* **119**, 391-410 (2013).

20 Penman, D. E., Hönisch, B., Zeebe, R. E., Thomas, E. & Zachos, J. C. Rapid and sustained surface ocean acidification during the Paleocene-Eocene Thermal Maximum. *Paleoceanography* **29**, 357-369 (2014).

21 Anagnostou, E. *et al.* Changing atmospheric CO_2 concentration was the primary driver of early Cenozoic climate. *Nature* **533**, 380–384 (2016).

22 Schubert, B. A. & Jahren, A. H. Reconciliation of marine and terrestrial carbon isotope excursions based on changing atmospheric CO_2 levels. *Nature Communications* **4**, Art. No. 1653 (2013).

23 Penman, D. E. *et al.* An abyssal carbonate compensation depth overshoot in the aftermath of the Palaeocene-Eocene Thermal Maximum. *Nature Geoscience* **9**, 575-580 (2016).

24 Turner, S. K. & Ridgwell, A. Development of a novel empirical framework for interpreting geological carbon isotope excursions, with implications for the rate of carbon injection across the PETM. *Earth and Planetary Science Letters* **435**, 1-13 (2016).

25 Röhl, U., Westerhold, T., Bralower, T. J. & Zachos, J. C. On the duration of the Paleocene-Eocene thermal maximum (PETM). *Geochemistry Geophysics Geosystems* **8**, Art. No. Q12002 (2007).

26 Svensen, H., Planke, S. & Corfu, F. Zircon dating ties NE Atlantic sill emplacement to initial Eocene global warming. *Journal of the Geological Society* **167**, 433-436 (2010).

27 Saunders, A. D. Two LIPs and two Earth-system crises: the impact of the North Atlantic Igneous Province and the Siberian Traps on the Earth-surface carbon cycle. *Geological Magazine* **153**, 201-222 (2016).

28 Rampino, M. R. Peraluminous igneous rocks as an indicator of thermogenic methane release from the North Atlantic Volcanic Province at the time of the Paleocene–Eocene Thermal Maximum (PETM). *Bulletin of Volcanology* **75**, 1-5 (2013).

29 Ma, Z. *et al.* Carbon sequestration during the Palaeocene-Eocene Thermal Maximum by an efficient biological pump. *Nature Geoscience* **7**, 382-388 (2014).

30 Dickson, A. J., Cohen, A. S. & Coe, A. L. Seawater oxygenation during the Paleocene-Eocene Thermal Maximum. *Geology* **40**, 639-642 (2012).

31 Jenkyns, H. C. Cretaceous anoxic events - from continents to oceans. *Journal of the Geological Society* **137**, 171-188 (1980).

32 Turner, S. K., Sexton, P. F., Charles, C. D. & Norris, R. D. Persistence of carbon release events through the peak of early Eocene global warmth. *Nature Geoscience* **7**, 748-751 (2014).

33 Payne, J. L. *et al.* Calcium isotope constraints on the end-Permian mass extinction. *Proceedings of the National Academy of Sciences* **107**, 8543-8548 (2010).

Acknowledgments

This study was funded by UK Ocean Acidification Research Program NERC / DEFRA / DECC grant NE/H017518/1 to P.N.P., G.L.F., and P.F.S. (which supported M.G.). A.R. was supported by a Heising-Simons Foundation award, and EU grant ERC 2013-CoG-617313. E.T. was in part supported by NSF OCE (grant no. NSF OCE 1536611). H.P. was in part supported by ERC Grant 2013-CoG-617462. This study used samples provided by the International Ocean Discovery Program (IODP). We thank Andy Milton at the University of Southampton for maintaining the mass spectrometers used in this study. Lulzim Haxhiaj at GEOMAR Kiel and Henning Kuhnert at MARUM Bremen are acknowledged for their help with carbon and oxygen isotope analyses.

Author contributions

G.L.F., P.F.S. and P.N.P. developed the concept and designed the study. M.G. and E.A. carried out the chemical sample preparation as well as elemental and isotopic analyses. P.F.S. performed the foraminifer taxonomy and prepared foraminifer samples for the analyses. R.D.N. and E.T. supplied washed coarse fraction samples. P.F.S. developed the age model. A.R. devised and conducted the Earth system modelling and analysis. H.P. carried out the carbon and oxygen isotopic analyses. M.G., A.R., G.L.F. and P.F.S. led the writing of the manuscript. All authors contributed to the interpretation and writing of the final text.

Methods

Site and sample selection

The open northeast Atlantic DSDP Site 401 (47° 25.65' N, 08° 48.62' W, 2495 m) was selected for this study. Its depth during the PETM was approximately 2000 m[34]. Around 2 mg of the 250-300 μm size fraction of mixed-layer dweller *Morozovella subbotinae* were picked for the carbon, oxygen and boron isotopic analyses. Furthermore, over the studied interval, very high-resolution $\delta^{18}O$ and $\delta^{13}C$ analyses of bulk carbonate were conducted to establish a revised age model for Site 401. Planktic foraminifera are extremely well preserved at Site 401[35], free from infilling and, particularly from the onset of the CIE upwards, are semi-glassy in appearance[36].

Sample treatment

Using a binocular microscope, picked foraminifera were cracked open under glass plates, the sample then homogenised, before splitting into a fraction for stable isotope ($\delta^{18}O$ and $\delta^{13}C$) analysis and another for the boron isotopic and elemental analyses (with a ratio of ca. 10:90). Purification and measurement of the boron fraction followed established protocols[37,38]. Samples were thoroughly cleaned to remove any adhering clays and samples were oxidatively cleaned using buffered peroxide in a warm water bath closely following[39]. Boron isotopic and elemental analyses were carried out on a Thermo Scientific Neptune MC-ICPMS and Element XR ICPMS, respectively, at the University of Southampton. Sample purification and handling was done in low-boron clean labs at the University of Southampton. The average boron total

procedural blank was on the order of 30 to 50 pg (n>10) and is hence negligible given our typical sample size (~5 to 15 ng of B). Boron isotopic uncertainties are reported at the 2 sigma level calculated using repeats of in-house carbonate standards[40]. Boron isotopic and elemental aliquots were measured using additional ammonia gas for better sample washout between samples and strictly monitored during every analytical session[37]. Prior to analysis for boron isotopic composition, samples were screened for chemical consistency by checking various elemental ratios (B/Ca, Mg/Ca, Al/Ca etc.) (Extended Data Fig. 1). While few samples had elevated Al/Ca (up to ~ 3400 μmol/mol) this feature did not translate into altered $\delta^{11}B$ (Extended Data Fig. 1).

Carbon and oxygen isotope aliquots were measured on a Thermo Finnigan MAT252 stable isotope mass spectrometer at the GEOMAR Helmholtz Centre for Ocean Research Kiel, Germany. Additionally, some foraminifera-based $\delta^{18}O$ and $\delta^{13}C$ analyses as well as all bulk carbonate stable isotope measurements were carried out at the MARUM Bremen, Germany on a Finnigan 251 gas isotope ratio mass spectrometer, coupled to a Kiel I automated carbonate preparation device. All produced isotope records are shown in Extended Data Fig. 2 plotted against depth in core. The carbon isotope excursion seen in our record is 3.4‰, significantly expanded relative to the benthic carbon isotope excursion presented by Nunes and Norris[41] that only reported an excursion on the order of 1.8‰. This discrepancy arises from the lower resolution data this earlier study[41] and the fact that samples were not taken through the core interval of the CIE at Site 401 (202.55 to 202.41 mcd) in this earlier study. We note that Bornemann et al.[35] reproduced a very similar magnitude of change in $\delta^{13}C$ to us; their $\delta^{13}C$ data obtained from the same species (*Morozovella subbotina*) registered a shift from 4.87‰ at 202.58 mcd to 1.47‰ at 202.46 mcd (an identical excursion magnitude of 3.4‰). The core containing the PETM (core 401-14) shows some rotary-drilling induced core deformation across the CIE. Such deformation commonly occurs across abrupt changes in lithology, but there is no obvious coring gap[35].

Effect of $\delta^{11}B$-pH calibration used on resulting pH excursion

Using the appropriate $\delta^{11}B$-pH calibration in order to convert calcite $\delta^{11}B$ into ambient seawater pH is essential for any paleo-pH reconstruction. For late Neogene studies using extant foraminifer species, the species used are typically calibrated for their $\delta^{11}B_{calcite}$ to pH dependency using culture or field studies[42,43] in order to assess the magnitude of $\delta^{11}B$-vital

effects that relate to foraminiferal physiology[44-46]. However, the species used here is extinct, making such calibrations impossible.

In order to bracket the likely magnitude of vital effects, and following ref. 21, we present two calibrations, one using the $\delta^{11}B$ to pH relationship of aqueous borate[47] and the other using the *T. sacculifer* calibration[43]. While the aqueous borate calibration is used for pH trends shown in Figs. 2 and 3, Extended Data Fig. 3a also present the alternative outcome. As noted previously[20,46], when pre-PETM pH is fixed (as is the case here), the choice of $\delta^{11}B$-pH calibration has little impact on the reconstructed pH curve. We note that the aqueous borate ion calibration is more conservative and is our preferred option. This is for the following reasons: (i) not all modern species show a reduced sensitivity to pH relative to aqueous borate[48]; (ii) previous studies have argued for a reduced magnitude of $\delta^{11}B$ vital effects in Eocene foraminifera.

$\delta^{18}O$ and Mg/Ca-based temperature reconstructions

M. subbotinae inhabited the surface ocean mixed layer and the temperatures used for determining pK^*_B (see Extended Data Fig. 8) were determined using the $\delta^{18}O_{calcite}$ to temperature relationship of inorganic carbonates[49] and a local NW Atlantic seawater $\delta^{18}O_{SMOW}$ of 0.014‰[50]. Mg/Ca based temperatures shown in Extended Data Fig. 8 were calculated using deep time foraminiferal Mg/Ca paleothermometry[51] using identical parameters as Dunkley-Jones et al.[2].

Determination of $\delta^{11}B_{sw}$

Boron in seawater has a residence time of between ~11 to 20 Ma[52,53] and to date the $\delta^{11}B_{sw}$ is not well constrained for the PETM. In order to create a self-consistent model-data setup we therefore used the output of GENIE ESM in the pre-CIE configuration which for the open NE Atlantic provides a pH of 7.75[6]. Using this pH information and employing the generic borate ion calibration[47] for the pH-dependent incorporation of boron into the studied foraminifera *Morozovella subbotinae* resulted in a $\delta^{11}B_{sw}$ of 38.94 ± 0.41‰. The uncertainty in deriving this bulk seawater $\delta^{11}B$ is based on 10,000 realizations of a borate ion to pH conversion using the commonly used experimentally derived boron fractionation factor[47], varying the given $\delta^{11}B$ randomly within its 2 sigma measurement uncertainty, and also varying salinity by ±1.5

392 psu and temperature by ±1.5°C. Utilising the *T. sacculifer* δ^{11}B-pH calibration[43], but
393 following the same approach, gives a $\delta^{11}B_{sw} = 37.6 \pm 0.5‰$.

394 **Chronology for Site 401**

395 A new and detailed age model was established for Site 401 by aligning our new ultra-high
396 resolution (1 cm-spacing) bulk carbonate δ^{18}O and δ^{13}C records with equivalent bulk
397 carbonate isotope records from Site 690 using the 'Analyseries' software[54]. Most stratigraphic
398 correlation tie points (vertical lines in Extended Data Fig. 4) were made using the δ^{18}O
399 records, which gave excellent agreement between the sites. The bulk δ^{18}O record from Site
400 401 shows high structural similarity to the δ^{18}O of the mixed layer-dwelling planktic
401 foraminifer *M. subbotinae* from this same site (Extended Data Fig. S2), and also to the δ^{18}O
402 of thermocline-dwelling *S. patagonica*[35], suggesting that bulk sediment δ^{18}O at Site 401
403 provides a reliable record of the basic trends in upper ocean warming and cooling across the
404 PETM. A dominant control by temperature on the bulk δ^{18}O signal makes sense, given the
405 scale of global surface ocean warming across the PETM[2] (4-5°C). The fidelity of the bulk
406 δ^{13}C record from Site 401 is supported by the fact that it shows high structural similarity to
407 the δ^{13}C of mixed layer-dwelling *M. subbotinae* (Extended Data Fig. S2), and also to the δ^{13}C
408 of thermocline-dwelling *S. patagonica*[35]. It is also consistent with bulk δ^{13}C from another
409 nearby location (the Forada section in northern Italy) that also shows an unusually early
410 recovery to higher δ^{13}C following the initial excursion to lowest δ^{13}C at the PETM's onset[55].
411 The Forada section is considered to be complete, because the CIE interval covers the
412 maximum number of precession cycles[25]. Site 690 currently has two detailed age models. By
413 detailed correlations to Site 401, we were thus able to transpose both the astronomically
414 calibrated chronology[25,56] and an extra-terrestrial He-based chronology[57] onto Site 401.
415 Extended Data Figs. 3b and c compares our pH record from Site 401 on both chronologies.
416 These uncertainties relating to choice of age model, and their impact on the calculated
417 duration of the onset phase, have been evaluated via modelling sensitivity experiments
418 (Extended Data Fig. S5) and have no impact on our main findings as discussed in the main
419 text.

420 A very different timescale for PETM carbon release during the CIE was suggested in an
421 earlier study, arguing for an onset of the PETM CIE within only 13 years[58]. The proposal of a
422 CIE onset within such a short timescale has proven controversial[59-63]. In particular,
423 geochemical modelling constraints[59] as well as drilling disturbance of the core creating the

impression of annual layering have together cast significant doubt on the suggested very rapid (~13 year) CIE onset. Indeed, Further Earth system model based analysis of the carbon and oxygen isotope records, leads to an estimate of 4 kyr or longer for PETM onset[64]. Given previously presented age constraints for the duration of the PETM CIE based on cyclostratigraphy[25] and a ^{3}He-based age model from ODP Site 690[57] in addition to absolute and cyclostratigraphic age constraints from Spitsbergen[16], we regard an age model that leads to a multi-millennia-scale CIE onset as more plausible. However, as analysed (Extended Data Fig. 5) and discussed earlier, assumptions regarding the duration of PETM onset interval itself are not critical to our conclusions.

Earth system modelling – configuration and data inversion methodology

(c)GENIE is an Earth system model of 'intermediate complexity'[65] comprising: a 3-D dynamic ocean circulation model with simplified energy-moisture balance atmosphere[66], a representation of the biogeochemical cycling of a variety of elements and isotopes in the ocean[67] including ^{13}C (see ref. 68 for a summary), plus representations of the preservation and burial of biogenic carbonates in accumulating marine sediments of the open ocean[68], and terrestrial weathering[69,70]. We utilize the cGENIE Earth system model in the same early Eocene configuration as recently employed[24,64] but with terrestrial weathering feedback enabled.

We introduce three separate model innovations here. The first builds on previous work[7,71] 'inverting' an observed δ^{13}C record to recover the underlying time-history of carbon release. In this, cGENIE adjusts mean atmospheric or surface ocean δ^{13}C to match a (proxy data) target at each model time-step (~1 week). If the current mean model value lies *above* the data value (observed data is automatically linearly interpolated to the model time-step), a pulse of carbon is released to the atmosphere (or ocean). If the model lies *below* the data value, depending on the experimental setup, carbon is either removed from the atmosphere, or nothing is done (cf. Fig. 3). The magnitude of the carbon pulse emitted at each time-step is prescribed and chosen such that the fastest observed change in δ^{13}C can be closely tracked, but without creating excessive overshoots in modelled δ^{13}C. Here, we allow a maximum rate of carbon emissions to the atmosphere of 10 PgC yr^{-1} and hence a magnitude of an individual pulse of ~0.21 PgC, corresponding to an instantaneous increase in atmospheric pCO_2 of about 0.1 ppm.

455 We diverge from an earlier approach[7,71] in that rather than utilizing a record of $\delta^{13}C$ as
456 our model target to assimilate, we instead employ our Site 401 reconstructed surface ocean
457 pH record. The methodology is inherently the same, but rather than comparing mean model
458 and observed $\delta^{13}C$ each time-step, we contrast (model and data) pH, diagnosing the required
459 carbon flux to the atmosphere in order that surface pH in the model tracks the data. The
460 model-data comparison is done on the basis of a mean global surface ocean pH value
461 calculated in cGENIE because utilizing a single (Site 401) surface ocean grid point in
462 cGENIE creates artefacts in the diagnosed carbon emissions because there is seasonality in
463 pH in the model but not in the data. We justify the assumption that proxy reconstructed
464 surface ocean pH at Site 401 can be representative of the global mean, firstly on the basis of
465 the relatively close degree of correspondence (visually) between the globally distributed pH
466 records available, as show in Fig. 2. Secondly, ocean surface pH, both today and during the
467 Paleocene–Eocene, is relatively uniform in the model (and supported by observations and
468 proxies, respectively), with maximum surface gradients between upwelling regions and sub-
469 polar regions of no more than 0.1 pH units for modern, and considerably less than this in the
470 late Paleogene (likely primarily due to the non-linear nature of the pH scale) (Extended Data
471 Fig. 6). Furthermore, these muted patterns are retained largely unaltered in response to CO_2
472 emissions. For instance, when we calculate the annual mean surface ocean pH anomaly at
473 different times across the PETM (experiment ID 'R07sm_Corg') as compared to the pre-
474 PETM pattern, we find a generally uniform (to within ±0.02 pH units) pattern in pH change
475 (Extended Data Fig. 6). If we contrast the evolution of global and annual mean surface ocean
476 pH across the PETM ('R07sm_Corg') with the annual mean surface pH at the location of Site
477 401 for the time points available (Extended Data Fig. 6, top), we also find Site 401 pH is
478 globally representative (and vice versa). All this goes to illustrate that there is unlikely to be
479 any substantive artefact in our assumption of treating our pH record at Site 401 as a surrogate
480 for the global mean in the model inversion experiment. Finally, and for comparison, a similar
481 analysis for the modern ocean under a future ocean acidification scenario (here, chosen to
482 follow RCP6.0[72]) is shown in Extended Data Fig. 6 and demonstrates a comparably spatially
483 uniform pattern of pH change.

484 The second innovation involves the determination of the $\delta^{13}C$ of the carbon emitted to
485 the atmosphere. Previously[7,71], the $\delta^{13}C$ of the carbon was treated as an unknown and a range
486 of different possible values (and hence carbon sources and reservoirs) tested in turn.
487 However, since observed pH constrains the magnitude of carbon emissions, we can now

simultaneously employ our observed $\delta^{13}C$ record to determine the source of carbon. The way in which the 'double inversion' methodology then works is that on each model time-step, following the assessment of whether or not a pulse of carbon is emitted to the atmosphere (based on the model-data pH difference), mean global model and observed Site 401 $\delta^{13}C$ values are compared. If the current mean model surface ocean $\delta^{13}C$ value lies *above* the current data value, the carbon emitted is assigned a carbon isotopic value of -100‰. If however, the mean model value lies *below* the data value, an isotopic value of 0‰ is assigned to the carbon values. By binning the emission fluxes in time and calculating a flux-weighted average $\delta^{13}C$, as per in Fig. 3, intermediate (between -100 and 0‰) $\delta^{13}C$ values are achieved. We emphasize that we are not assuming a source that could be -100‰ *per se* – this choice of extremely depleted value simply gives the model greater flexibility in tracking the trend in $\delta^{13}C$ emissions – isotopically intermediate mean annual carbon emissions arise by varying proportions of individual 0‰ and -100‰ carbon pulses. We could have used any value just as long as it is as least as light as the lightest potential source (e.g. -60‰).

Finally, in the situation that the mean model surface ocean $\delta^{13}C$ value becomes lower than the observed Site 401 value, we also test the importance of marine organic carbon (C_{org}) burial. This works identically to the negative emissions diagnosed in previous studies[7,71] (when carbon is removed from the system to force $\delta^{13}C$ more positive) but rather than prescribing the $\delta^{13}C$ value, we calculate it according to a simple phytoplankton organic matter fractionation scheme[67,73].

For all our experiments, we first spun up the model under late Paleocene boundary conditions[24,64], here choosing an open system run time of 200 kyr in order to fully bring the long-term $\delta^{13}C$ cycle into balance (and following on from an initially closed system spin-up of 20 kyr used to established the basic climate and ocean circulation state). We then carried out a range of experiments as summarized in Extended Data Table 1a. We tested combinations (not all are reported here) of: (i) age model – orbital cyclostratigraphy ('R07') vs. ^{3}He-based age model ('FE'), uncertainty in the pH reconstruction – mean vs. the 2.5% and 97.5% confidence limits ('LO' and 'HI', respectively), whether or not the data is smoothed ('sm') or raw ('rw'), whether or not climate-dependent weathering feedback was allowed, or weathering was fixed ('noW'), and whether or not C_{org} burial was enabled to recover $\delta^{13}C$ to more positive (and data tracking) values (*Corg* when carbon burial was enabled). These experiments were run for 500 kyr, with the exception of the carbon burial *Corg* series of experiments (Extended Data Table 1a), which were run for an initial interval of 72.6 kyr and

up until the peak of the CIE with no organic carbon burial allowed, and then a further 227.4 kyr with carbon burial allowed when needed (for a total of 300 kyr of simulation). Model results are plotted relative to the observed data point defining PETM onset.

Earth system modelling – additional sensitivity experiments and analysis

We also carried out a range of sensitivity experiments to explore the importance (or otherwise) of the assumed duration of the CIE onset – in other words, whether there is a strong age model dependence of diagnosed total carbon emissions. In this series of experiments, the CIE onset phase was assumed to occur as a simultaneous linear decline in both $\delta^{13}C$ (by -3.5‰) and pH (by -0.3 pH units). We varied the duration of this decline from 100 to 20,000 yr. Once the minimum in $\delta^{13}C$ and pH was reached, these values were held constant up until the end of the experiment (a total of 50 kyr). The exact same double inversion methodology was employed and starting from the same spin-up state as the main experiments. The results of these sensitivity experiments are plotted in Extended Data Fig. 5 and summarised in Extended Data Table 1b.

Further details of the model and its paleo configuration, plus comprehensive discussion of model uncertainties, can be found in the supplementary information file SI 1. Additional assessments of the evolution of model-projected global mean as well as spatial patterns of sedimentary wt% $CaCO_3$ and sea-surface temperature are illustrated in Extended Data Figs. 7 and 8, respectively (and described in SI). Site-specific model-data comparisons are shown in Extended Data Fig. 9 (and again discussed in full in SI 1).

Earth system modelling – model code and supporting file availability

The source code of the cGENIE Earth system model used to generate the results presented in this paper, together with specific experiment configuration, boundary conditions, and data-forcing files, is available for download. A brief overview of and directions to: obtaining the code and configuring the cGENIE Earth system model, basic usage of the cGENIE Earth system model and required software, plus details of and how to execute and analyse the published model experiments, is given here: http://www.seao2.info/cgenie/pubs/gutjahretal.2017.txt Further specific details of e.g. using the provided plotting functions to process the model results as per in the paper, configurations for the experiments presented in Extended Data and/or described in the SI, or the raw model output, can be obtained directly from A.R. (andy@seao2.org).

Data availability

Foraminifera and bulk carbonate stable isotope results are published alongside this articles in Supplementary Tables S1 and S2 and can also be accessed on the UK National Geoscience Data Centre (NGDC) (http://www.bgs.ac.uk/services/ngdc/). All modeling related data is included as part of the cGENIE model code distribution (see above).

Competing financial interests

The authors declare no competing financial interests.

34 Pardo, A., Keller, G., Molina, E. & Canudo, J. I. Planktic foraminiferal turnover across the Paleocene-Eocene transition at DSDP site 401, Bay of Biscay, North Atlantic. *Marine Micropaleontology* **29**, 129-158 (1997).

35 Bornemann, A. *et al.* Persistent environmental change after the Paleocene-Eocene Thermal Maximum in the eastern North Atlantic. *Earth and Planetary Science Letters* **394**, 70-81 (2014).

36 Sexton, P. F., Wilson, P. A. & Pearson, P. N. Microstructural and geochemical perspectives on planktic foraminiferal preservation: "Glassy" versus "Frosty". *Geochemistry Geophysics Geosystems* **7**, Art. No. Q12P19 (2006).

37 Foster, G. L. Seawater pH, pCO_2 and $[CO_3^{2-}]$ variations in the Caribbean Sea over the last 130 kyr: A boron isotope and B/Ca study of planktic forminifera. *Earth and Planetary Science Letters* **271**, 254-266 (2008).

38 Foster, G. L. *et al.* Interlaboratory comparison of boron isotope analyses of boric acid, seawater and marine $CaCO_3$ by MC-ICPMS and NTIMS. *Chemical Geology* **358**, 1-14 (2013).

39 Barker, S., Greaves, M. & Elderfield, H. A study of cleaning procedures used for foraminiferal Mg/Ca paleothermometry. *Geochemistry Geophysics Geosystems* **4**, Art. No. 8407 (2003).

40 Henehan, M. J. *et al.* Calibration of the boron isotope proxy in the planktonic foraminifera Globigerinoides ruber for use in palaeo-CO_2 reconstruction. *Earth and Planetary Science Letters* **364**, 111-122 (2013).

41 Nunes, F. & Norris, R. D. Abrupt reversal in ocean overturning during the Palaeocene/Eocene warm period. *Nature* **439**, 60-63 (2006).

42 Sanyal, A., Bijma, J., Spero, H. & Lea, D. W. Empirical relationship between pH and the boron isotopic composition of Globigerinoides sacculifer: Implications for the boron isotope paleo-pH proxy. *Paleoceanography* **16**, 515-519 (2001).

43 Martinez-Boti, M. A. *et al.* Boron isotope evidence for oceanic carbon dioxide leakage during the last deglaciation. *Nature* **518**, 219-222 (2015).

44 Zeebe, R. E., Wolf-Gladrow, D. A., Bijma, J. & Hönisch, B. Vital effects in foraminifera do not compromise the use of delta B-11 as a paleo-pH indicator: Evidence from modeling. *Paleoceanography* **18**, Art. No. 1043 (2003).

45 Hönisch, B. *et al.* The influence of symbiont photosynthesis on the boron isotopic composition of foraminifera shells. *Marine Micropaleontology* **49**, 87-96 (2003).

46 Foster, G. L. & Rae, J. W. B. Reconstructing ocean pH with boron isotopes in foraminifera. *Annual Review of Earth and Planetary Sciences* **44**, 207-237 (2016).

47 Klochko, K., Kaufman, A. J., Yao, W. S., Byrne, R. H. & Tossell, J. A. Experimental measurement of boron isotope fractionation in seawater. *Earth and Planetary Science Letters* **248**, 276-285 (2006).

48 Henehan, M. J. *et al.* A new boron isotope-pH calibration for Orbulina universa, with implications for understanding and accounting for 'vital effects'. *Earth and Planetary Science Letters* **454**, 282-292 (2016).

49 Kim, S.-T. & O'Neil, J. R. Equilibrium and nonequilibrium oxygen isotope effects in synthetic carbonates. *Geochimica et Cosmochimica Acta* **61**, 3461-3475 (1997).

50 Tindall, J. *et al.* Modelling the oxygen isotope distribution of ancient seawater using a coupled ocean-atmosphere GCM: Implications for reconstructing early Eocene climate. *Earth and Planetary Science Letters* **292**, 265-273 (2010).

51 Evans, D. & Müller, W. Deep time foraminifera Mg/Ca paleothermometry: Nonlinear correction for secular change in seawater Mg/Ca. *Paleoceanography* **27**, Art. No. PA4205 (2012).

52 Spivack, A. J. & Edmond, J. M. Boron isotope exchange between seawater and the oceanic crust. *Geochimica et Cosmochimica Acta* **51**, 1033-1043 (1987).

53 Lemarchand, D., Gaillardet, J., Lewin, E. & Allegre, C. J. Boron isotope systematics in large rivers: implications for the marine boron budget and paleo-pH reconstruction over the Cenozoic. *Chemical Geology* **190**, 123-140 (2002).

54 Paillard, D., Labeyrie, L. & Yiou, P. Macintosh program performs time‐series analysis. *Eos, Transactions American Geophysical Union* **77**, 379-379 (1996).

55 Giusberti, L. *et al.* Mode and tempo of the Paleocene-Eocene thermal maximum in an expanded section from the Venetian pre-Alps. *Geological Society of America Bulletin* **119**, 391-412 (2007).

56 Röhl, U., Bralower, T. J., Norris, R. D. & Wefer, G. New chronology for the late Paleocene thermal maximum and its environmental implications. *Geology* **28**, 927-930 (2000).

57 Farley, K. A. & Eltgroth, S. F. An alternative age model for the Paleocene-Eocene Thermal Maximum using extraterrestrial He-3. *Earth and Planetary Science Letters* **208**, 135-148 (2003).

58 Wright, J. D. & Schaller, M. F. Evidence for a rapid release of carbon at the Paleocene-Eocene thermal maximum. *Proceedings of the National Academy of Sciences* **110**, 15908-15913 (2013).

59 Zeebe, R. E., Dickens, G. R., Ridgwell, A., Sluijs, A. & Thomas, E. Onset of carbon isotope excursion at the Paleocene-Eocene thermal maximum took millennia, not 13 years. *Proceedings of the National Academy of Sciences* **111**, E1062-E1063 (2014).

60 Pearson, P. N. & Nicholas, C. J. Layering in the Paleocene/Eocene boundary of the Millville core is drilling disturbance. *Proceedings of the National Academy of Sciences* **111**, E1064-E1065 (2014).

61 Stassen, P., Speijer, R. P. & Thomas, E. Unsettled puzzle of the Marlboro clays. *Proceedings of the National Academy of Sciences* **111**, E1066-E1067 (2014).

62 Wright, J. D. & Schaller, M. F. Reply to Pearson and Nicholas, Stassen et al., and Zeebe et al.: Teasing out the missing piece of the PETM puzzle. *Proceedings of the National Academy of Sciences* **111**, E1068-E1071 (2014).

63 Pearson, P. N. & Thomas, E. Drilling disturbance and constraints on the onset of the Paleocene–Eocene boundary carbon isotope excursion in New Jersey. *Clim. Past* **11**, 95-104 (2015).

64 Zeebe, R. E., Ridgwell, A. & Zachos, J. C. Anthropogenic carbon release rate unprecedented during the past 66 million years. *Nature Geoscience* **9**, 325–329 (2016).

65 Brady, P. V. The effect of silicate weathering on global temperature and atmospheric CO_2. *Journal of Geophysical Research* **96**, 18101-18106 (1991).

66 Edwards, N. R. & Marsh, R. Uncertainties due to transport-parameter sensitivity in an efficient 3-D ocean-climate model. *Clim. Dyn.* **24**, 415-433 (2005).

67 Ridgwell, A. *et al.* Marine geochemical data assimilation in an efficient Earth System Model of global biogeochemical cycling. *Biogeosciences* **4**, 87-104 (2007).

68 Ridgwell, A. & Hargreaves, J. C. Regulation of atmospheric CO_2 by deep-sea sediments in an Earth system model. *Glob. Biogeochem. Cycle* **21**, Art. No. GB2008 (2007).

69 Colbourn, G., Ridgwell, A. & Lenton, T. M. The time scale of the silicate weathering negative feedback on atmospheric CO_2. *Glob. Biogeochem. Cycle* **29**, 583-596 (2015).

70 Lord, N. S., Ridgwell, A., Thorne, M. C. & Lunt, D. J. The 'long tail' of anthropogenic CO_2 decline in the atmosphere and its consequences for post-closure performance assessments for disposal of radioactive wastes. *Mineralogical Magazine* **79**, 1613-1623 (2015).

71 Cui, Y. & Kump, L. R. Global warming and the end-Permian extinction event: Proxy and modeling perspectives. *Earth-Science Reviews* **149**, 5-22 (2015).

72 IPCC. *Climate Change 2013: The physical science basis. Contribution of working group I to the fifth assessment report of the intergovernmental panel on climate change*. 1-1535 (eds T. F. Stocker *et al.*) (2013).

73 Ridgwell, A. *Glacial-interglacial perturbations in the global carbon cycle* PhD thesis, Univ. of East Anglia at Norwich, UK, (2001).

74 Cao, L. *et al.* The role of ocean transport in the uptake of anthropogenic CO_2. *Biogeosciences* **6**, 375-390 (2009).

Manuscript Figure Captions

Fig. 1. New DSDP Site 401 stable isotope data. Foraminifera (*M. subbotinae*) (a) and bulk carbonate $\delta^{13}C$ (b), $\delta^{11}B$ (c) and $\delta^{18}O$ (d and e) records plotted relative to the onset of the PETM carbon isotope excursion (CIE) from DSDP Site 401 (47° 25.65' N, 08° 48.62' W, 2495 m) using our preferred age model (see Methods).

Fig. 2. *M. subbotinae* based $\delta^{13}C$ and boron isotope based pH reconstructions of Site 401. Panels A and B show the entire record, while C and D focus on the CIE interval. Also shown are data of ref. 20 on the original age model with pH values recalculated using a laboratory offset such that pre-PETM pH calculated using our Monte Carlo approach at Site 1209 = 7.74 given the distribution of seawater $\delta^{11}B$ determined at Site 401 (38.9 ± 0.4‰). This resulted in a mean correction of the literature data[20] of -0.32‰.

Fig. 3. Results of Earth system model data assimilation. The right hand panels also account for organic carbon burial during PETM recovery. (a,i) Atmospheric pCO_2 (red, LH axis) and mean global SST (blue, RH axis). (b,j) Modelled mean global ocean surface pH (observed smoothed surface ocean pH data as yellow symbols). (c,k) Model diagnosed rates of CO_2 release (red) and excess CO_2 consumption due to silicate weathering (green) from PETM onset onwards. (d,l) Cumulative CO_2 release (red) and organic carbon burial (blue). (e,m) Modelled mean global ocean surface $\delta^{13}C$ (observations as yellow symbols). (f,n) Model diagnosed $\delta^{13}C$ of the CO_2 release (red) and isotopic composition of buried carbon (blue). Shaded bands (a,b,e,i,j,m) and empty bars (c,d,f,k,l,n) reflect 95% uncertainty limits. Bars reflect 2 kyr averaging (c,f,k,n) or integration (d,l) bins. All model results and related data are plotted from -50 to +150 kyr relative to the onset of the CIE, on our preferred orbital age model[25].

693 **Extended Data Figure Captions**

694 **Extended Data Fig. 1. Elemental and stable isotope cross-plots for *M. subbotinae***
695 **measured in this study.**

696 **Extended Data Fig. 2. Foraminifera- and bulk carbonate stable isotope data plotted**
697 **against depth in core.** Foraminifera-based stable isotope compositions were generated from
698 identical samples after splitting of $\delta^{13}C$ / $\delta^{18}O$ fraction from the $\delta^{11}B$ fraction.

699 **Extended Data Fig. 3. Illustration of $\delta^{11}B$ to pH conversion as well as age model**
700 **differences.** (a) Comparison of pH evolution at Site 401 over the PETM CIE using either the
701 borate ion[47] (red) or alternatively the *T. sacculifer*[43] (green) calibration. Age scale used is
702 following Röhl et al.[25]. (b) Direct comparison of our two age models, showing the
703 reconstructed pH evolution of Site 401 plotted using either the age model of Farley and
704 Eltgroth[57] or our preferred age model of Röhl et al.[25]. (c) Expanded view of (b).

705 **Extended Data Fig. 4. Selection of age model tie points.** Bulk carbonate $\delta^{13}C$ and $\delta^{18}O$
706 comparison between Site 401 and Site 690 presented in Röhl et al.[25]. Vertical lines highlight
707 age tie points used to derive the age model relative to the PETM carbon isotope excursion
708 (see methods for discussion).

709 **Extended Data Fig. 5. Key results of sensitivity experiments.** Illustrating the influence of
710 uncertainties in the CIE onset duration on diagnosed total carbon release. In these idealized
711 experiments, the CIE onset phase is assumed to occur linearly, with a duration of the decline
712 in $\delta^{13}C$ (by 3.5‰) and pH (by 0.3 pH units) that varies from 100 to 20,000 yr, with the target
713 pH and $\delta^{13}C$ values thereafter held constant until the end of the experiment (50,000 yr). The
714 evolution with time of these target ocean surface variables is shown in the uppermost panels
715 (a), with pH on the left hand y-axis, and $\delta^{13}C$ on the right hand y-axis. The lower rows of
716 panels show: (b) maximum emission rate per time interval, (c) cumulative carbon emission
717 for respective onset phase in EgC (1 Eg = 10^{18} g) and (d) average emitted $\delta^{13}C$ per time
718 interval.

Extended Data Fig. 6. Spatial and temporal evolution of mean annual surface ocean pH in cGENIE. Illustrated both across the PETM and for comparison, modern pH patterns projected from preindustrial and into the future under RCP 6.0[72]. Shown are: (a) Global and annual mean surface ocean pH (black solid line) across the PETM from experiment 'R07sm_Corg' (our central pH estimate, using the inorganic borate ion calibration and the RH07 age model, and including an assumption of organic carbon burial post peak PETM). Red circles represent the annual mean pH values at the location of Site 401 in the model (see location in panel b) taken at times in the model simulation that have a corresponding $\delta^{11}B$ derived pH data points (cf. Fig. 3b) (but note that we do not utilize all of the observed data points). (b) Model projected spatial pattern of annual mean surface ocean pH at time zero (i.e. PETM onset). (c-f) Model projected spatial pattern of the annual mean surface ocean pH anomaly compared to time zero, for the highlighted time-points in (a) – 5.0, 31.6, 58.2, and 71.5 kyr following onset. (g) Model projected spatial pattern of annual mean surface ocean pH in the modern ocean under pre-industrial atmospheric CO_2 (278 ppm). The model is configured as per described in *Cao et al.*[74] and driven with a CO_2 emissions scenario calculated consistent with RCP 6.0. (h-i) Model projected spatial pattern of the annual mean surface ocean pH anomaly compared to 1765, at year 2010 and 2050. The scale is chosen to be the same as per (c-f).

Extended Data Fig. 7. Spatial and temporal evolution of surface sedimentary carbonate content in cGENIE across the PETM. (a) Global mean surface sedimentary wt% $CaCO_3$ (black solid line) across the PETM from experiment 'R07sm_Corg'. White circles represent the times from PETM onset onwards that correspond to the $\delta^{11}B$ derived pH data points as per in Fig. 3b and Extended Data Fig. 6. Note that the white circles do not represent 'values' and are plotted simply as markers of specific time-points (see Extended Data Fig. 6). (b) Model projected spatial pattern of surface sedimentary wt% $CaCO_3$ at time zero (i.e. PETM onset). Shown are the locations of sites for which surface ocean pH has been reconstructed (see Fig. 2) and at which detailed down-core model-data comparison is carried out (Extended Data Fig. 9). (c-f) Model projected spatial pattern of the surface sedimentary wt% $CaCO_3$ anomaly compared to time zero, for the highlighted time-points in (a) – 5.0, 31.6, 58.2, and 71.5 kyr following onset. (g) For reference – the assumed seafloor bathymetry in the model (together with the locations of the four data-rich sites focussed on in the SI analysis).

Extended Data Fig. 8. Spatial and temporal evolution of sea surface temperature in cGENIE across the PETM. (a) Global and annual mean sea surface temperature (SST) (black solid line) across the PETM from experiment 'R07sm_Corg'. Yellow circles represent the annual mean SST values at the location of Site 401 in the model at the times from PETM onset onwards that correspond to the $\delta^{11}B$ derived pH data points (cf. Fig. 3b). Orange and blue filled circles represent Mg/Ca and $\delta^{18}O$ derived, respectively, SST estimates. (b) Model projected spatial pattern of annual mean SST at time zero. The location of Site 401 in the model is highlighted by a star. (c-f) Model projected spatial pattern of the annual mean SST anomaly compared to time zero, for the highlighted time-points in (a) (yellow circles) – 5.0, 31.6, 58.2, and 71.5 kyr following onset.

Extended Data Fig. 9. Down-core model-data evaluation at four data-rich sites. Shown are comparisons for four ocean drilling sites for which surface ocean pH has been reconstructed across the PETM (Fig. 2) – 401, 865, 1209, and 1263 (this study and ref. 20). Their paleo locations in the cGENIE Earth system model are shown to the side (panel q). Model-data comparisons are made for: (i) wt% $CaCO_3$ (far LH panel for each site), (ii) $\delta^{13}C$ of bulk carbonate (second-from-left series of panels), and (iii) surface ocean pH (third-from-left series of panels). To provide an orientation in time with regard to the evolution across the PETM event, the farthest-right series of panels shows the projected evolution of atmospheric $\delta^{13}C$ of CO_2 in the model. For wt% $CaCO_3$ and $\delta^{13}C$ of bulk carbonate, model points (resolved at 1 cm resolution) are plotted as filled yellow circles. Model-projected pH (global and annual mean, as per shown in Fig. 3j and Extended Data Fig. 6a) and atmospheric $\delta^{13}C$ of CO_2 are shown as continuous red lines. In all cases, observed data values are shown as stars (*). The age models for Sites 865, 1209 and 1263 employing original relative age model constraints[20] used to convert from model-simulated sediment depth (resolved at 1 cm intervals) at each location in the cGENIE Earth system model, are calculated using a constant detrital flux accumulation rate. The observed data are plotting on their respective site 690-derived age models[25]. Both model and data age scales are synchronized to age zero at PETM onset (horizontal line). See SI for details.

Extended Data Table 1. Key results from individual model runs. (a) Summary of the main double inversion experiments carried out. The terminology "R07" refers to configurations tying the Site 401 records to the chronostratigraphy of ref. 25, the notation "FE" refers to the

^{3}He-based age model of ref. 57). Annotation "sm" refers to inversion of analytically smoothed $\delta^{13}C$ and pH data sets, "rw" to usage of original sample data for double inversions. "HI" and "LO" represent potentially extreme configurations taking into account the boron proxy uncertainty at 95% confidence level. "noW" has silicate (and carbonate) weathering feedbacks disabled. "Corg" denote model configurations that allow removal of excess organic carbon from the surface ocean. Grey shading highlights experiments focussed upon in the main text and plotted in Figure 3 ("R07sm" in Fig. 3a-f and "R07sm_Corg" in 3i-n.). Note: (1) peak emissions are binned at 2 kyr resolution, (2) both cumulative emissions and C_{org} burial are measured from 40 to 190 ka model time, and (3) peak excess weathering reflects carbon removal due to silicate weathering above pre-PETM weathering rates. (b) Summary table presenting the results of sensitivity experiments (shown in Extended Data Fig. 5) to quantify the importance of uncertainties in the age model for the CIE onset. In these experiments, the CIE onset phase is assumed to occur linearly, with a duration of the decline in $\delta^{13}C$ and pH varying from 100 to 20,000 yr duration. Reported are: (1) diagnosed peak carbon emissions, (2) cumulative carbon emissions occurring over the duration of the onset, and mean (flux weighted) $\delta^{13}C$ of these emissions, (3) cumulative carbon emissions occurring at the 20 kyr time horizon – comparable to the onset duration in our assumed age model, plus the mean (flux weighted) $\delta^{13}C$ of these emissions, and (4) the cumulative carbon emissions occurring at the 20 kyr horizon, plus the mean (flux weighted) $\delta^{13}C$ of these emissions. Note that in all experiments, once the onset is complete, the target pH and $\delta^{13}C$ values are held constant (and low) until the end of the experiment (50,000 yr).

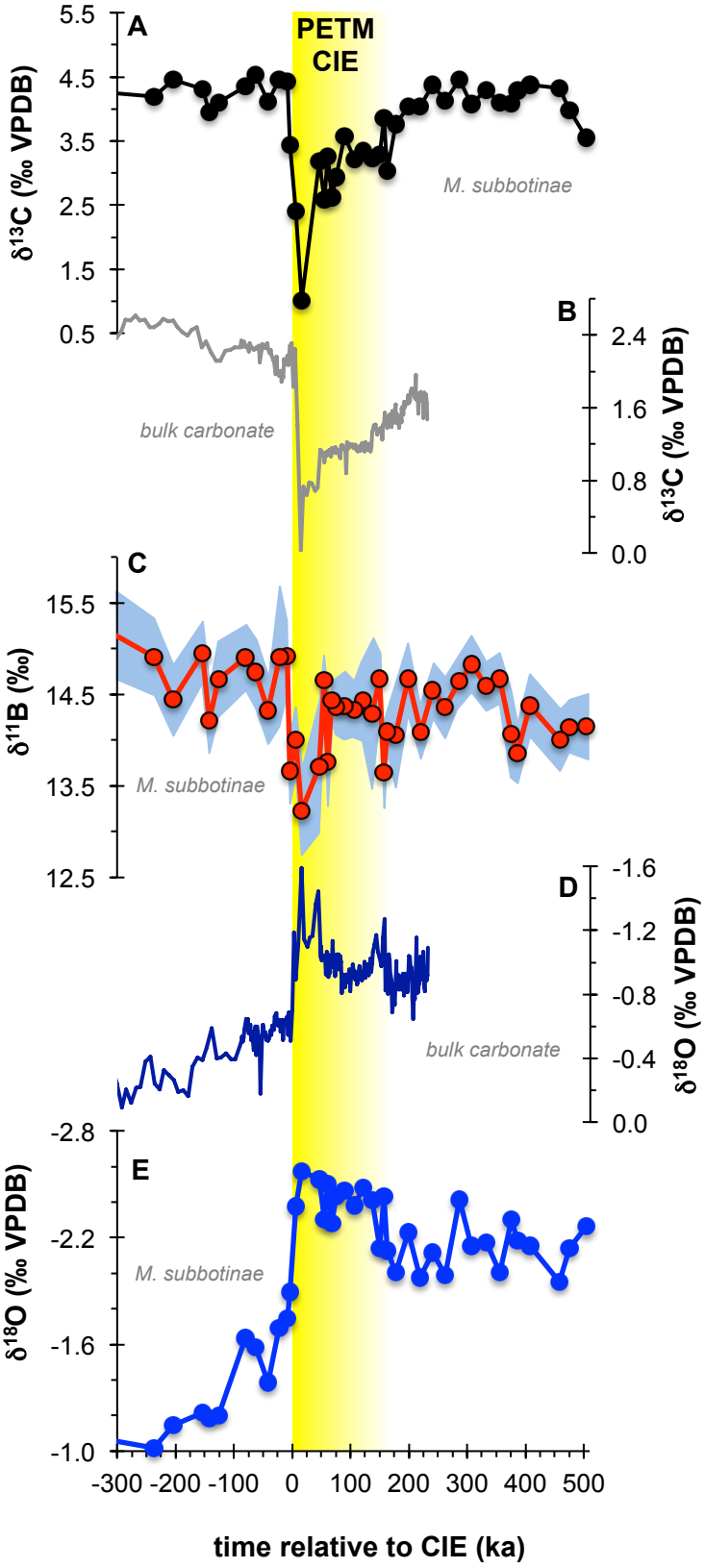
A
PETM
CIE
M. subbotinae
B
bulk carbonate
C
M. subbotinae
D
bulk carbonate
E
M. subbotinae
δ13C (‰ VPDB)
δ11B (‰)
δ18O (‰ VPDB)
5.5
4.5
3.5
2.5
1.5
0.5
2.4
1.6
0.8
0.0
15.5
14.5
13.5
12.5
-1.6
-1.2
-0.8
-0.4
0.0
-2.8
-2.2
-1.6
-1.0
-300 -200 -100 0 100 200 300 400 500
time relative to CIE (ka)

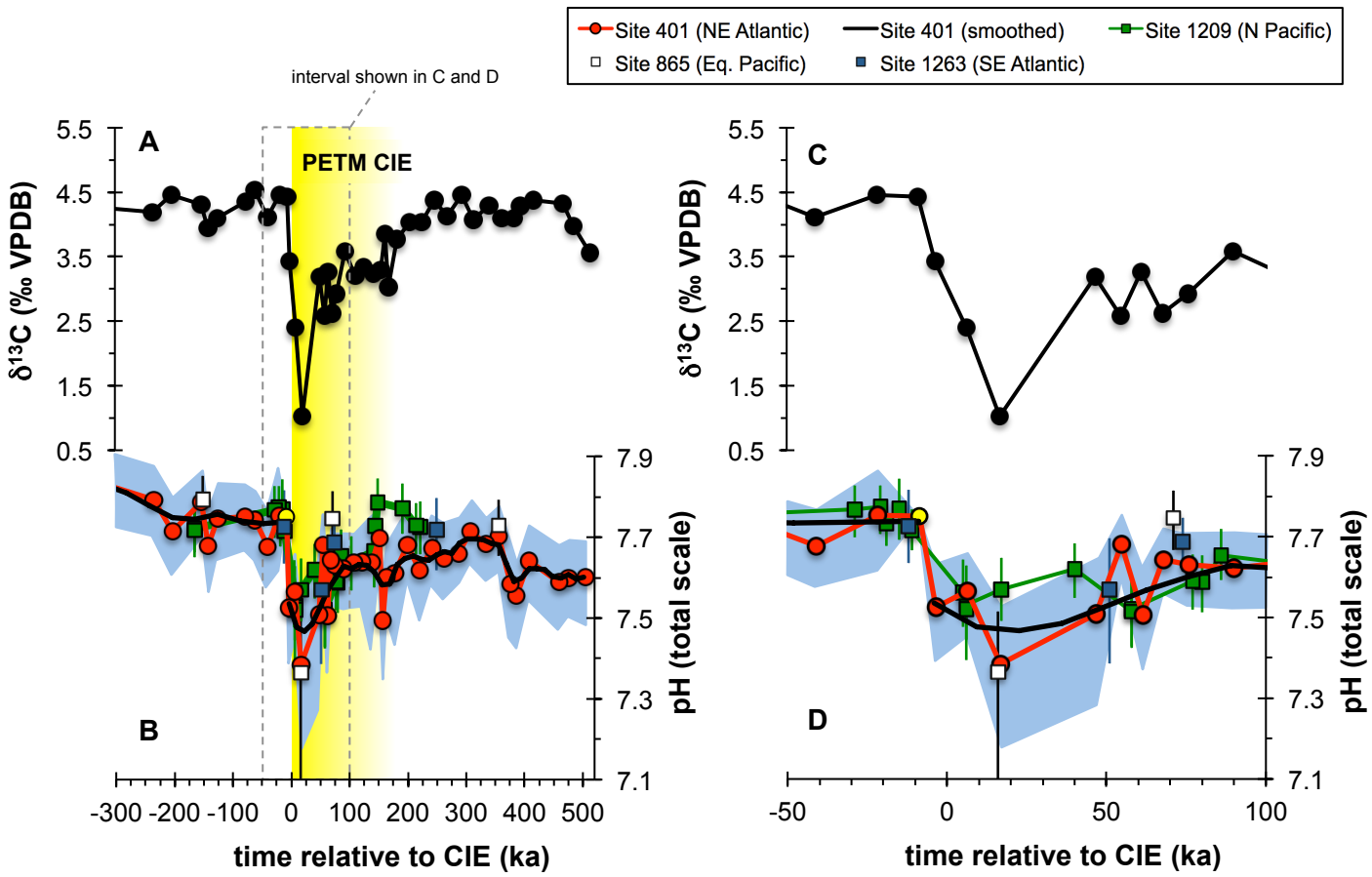
Site 401 (NE Atlantic)
Site 401 (smoothed)
Site 1209 (N Pacific)
Site 865 (Eq. Pacific)
Site 1263 (SE Atlantic)
interval shown in C and D
A
PETM CIE
B
C
D
δ13C (‰ VPDB)
pH (total scale)
time relative to CIE (ka)
time relative to CIE (ka)

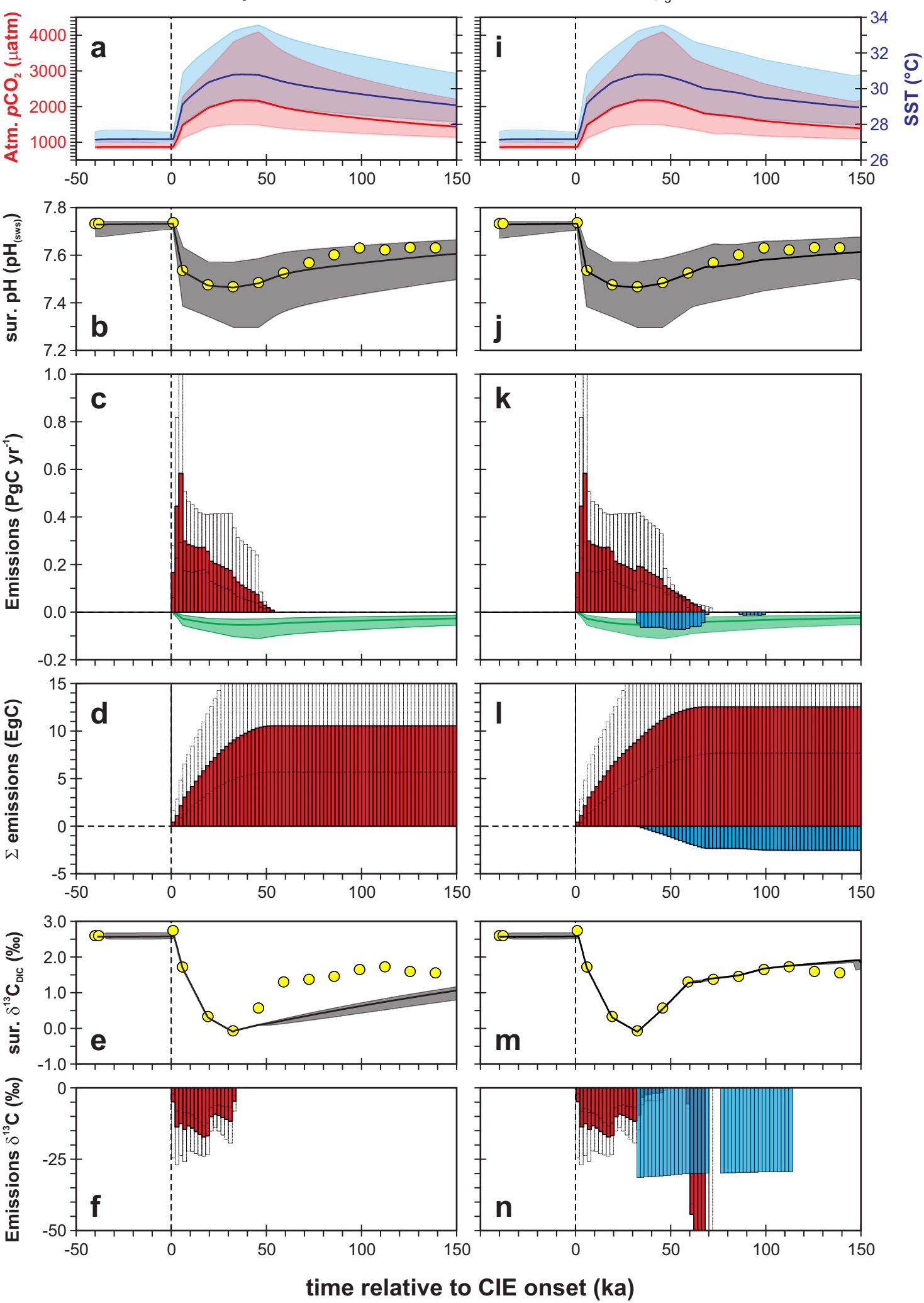
Emissions only
Emissions + C$_{org}$ burial
Atm. pCO$_2$ (µatm)
SST (°C)
sur. pH (pH$_{(sws)}$)
Emissions (PgC yr^{-1})
Σ emissions (EgC)
sur. δ^{13}C$_{DIC}$ (‰)
Emissions δ^{13}C (‰)
time relative to CIE onset (ka)
a
b
c
d
e
f
i
j
k
l
m
n

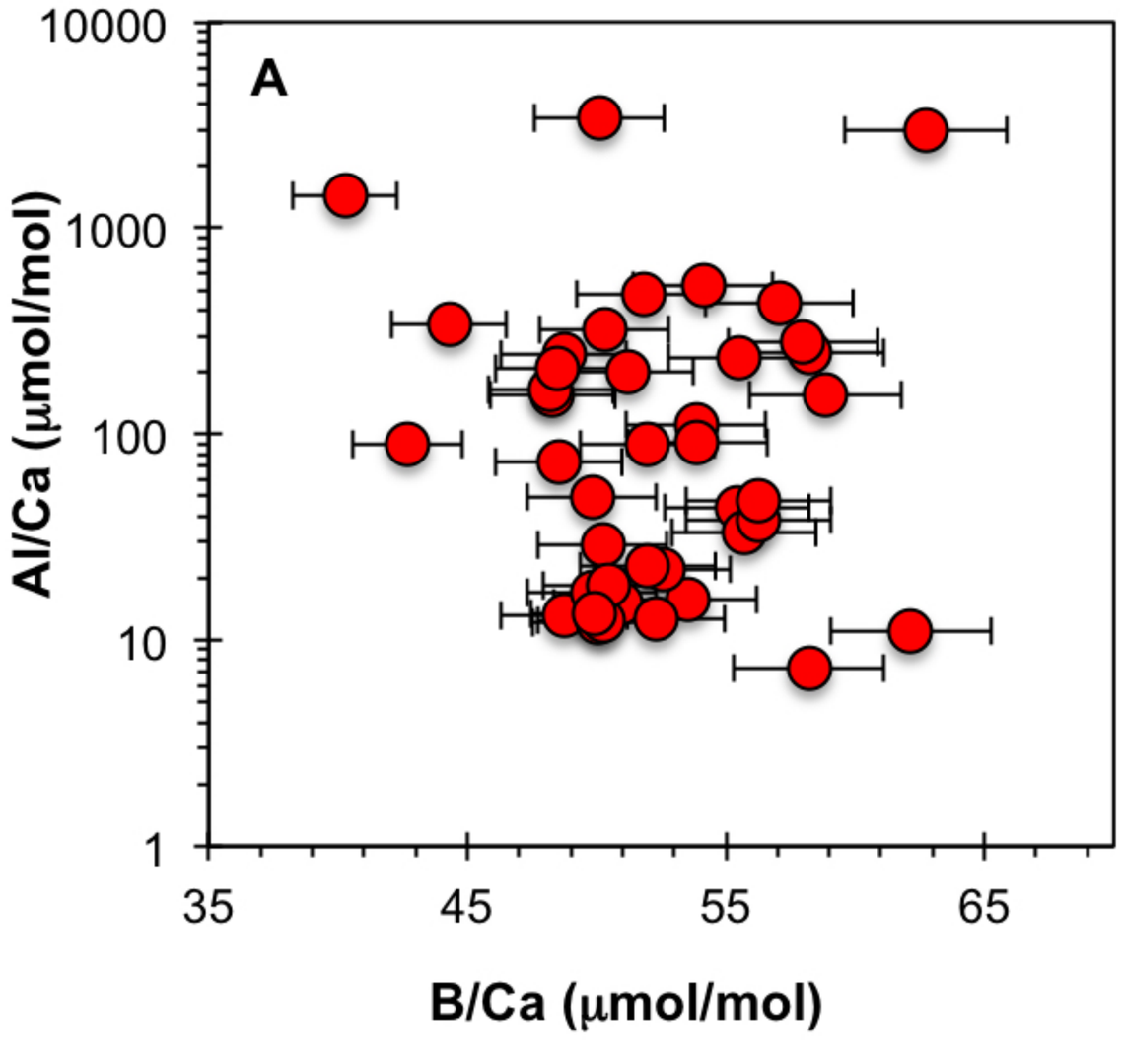
A
Al/Ca (µmol/mol)
10000
1000
100
10
1
35
45
55
65
B/Ca (µmol/mol)

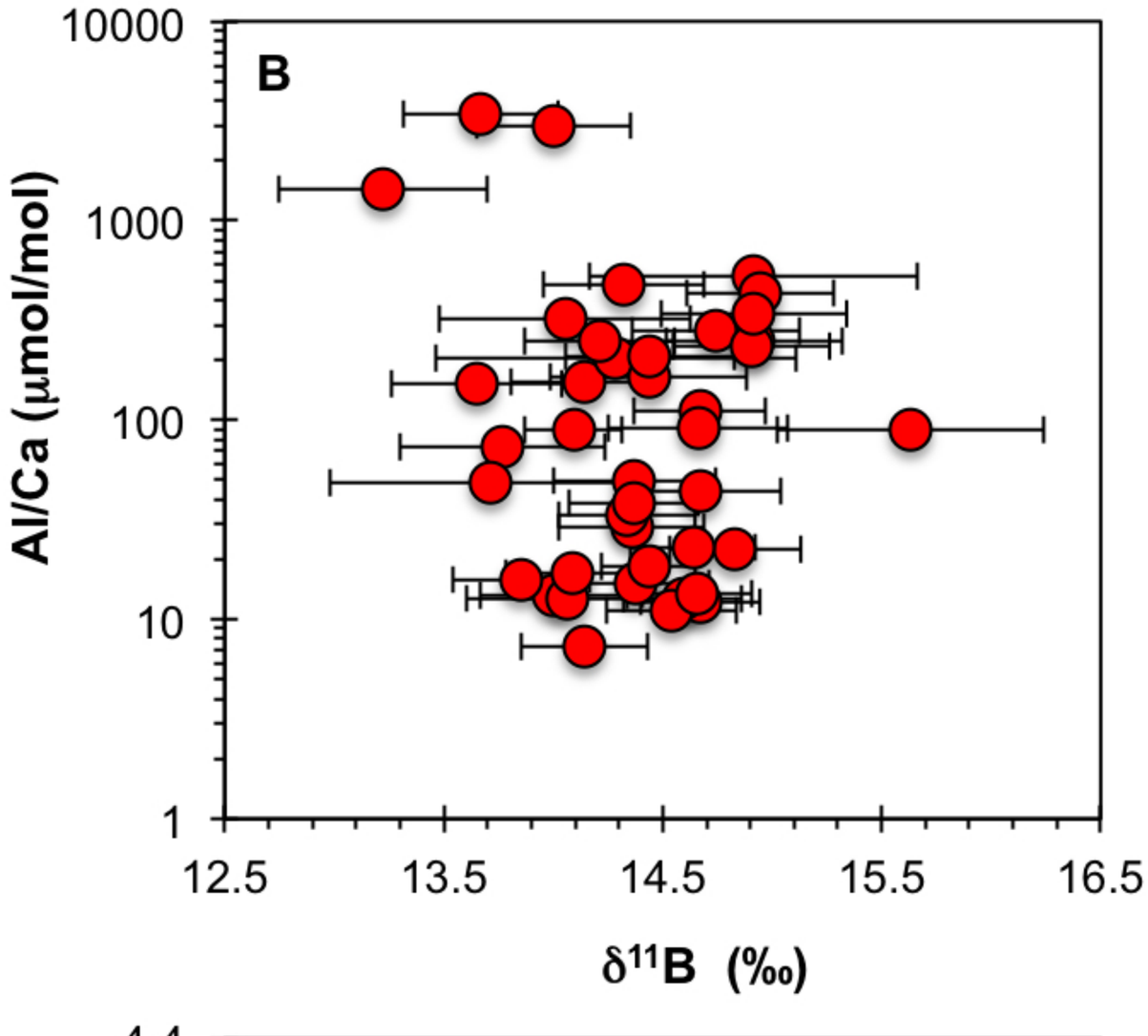
B
Al/Ca (µmol/mol)
10000
1000
100
10
1
12.5
13.5
14.5
15.5
16.5
δ11B (‰)

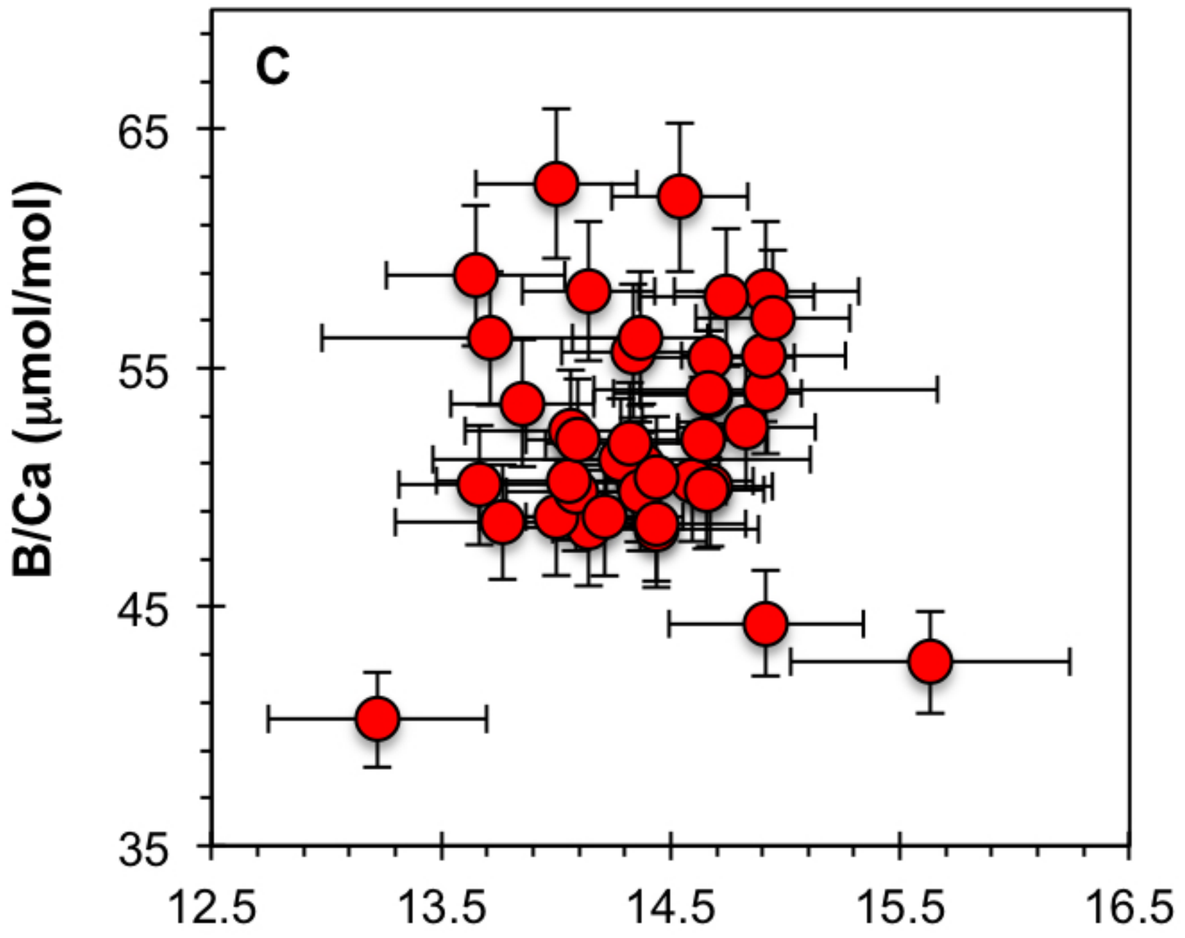
C
B/Ca (µmol/mol)
65
55
45
35
12.5
13.5
14.5
15.5
16.5
δ11B (‰)

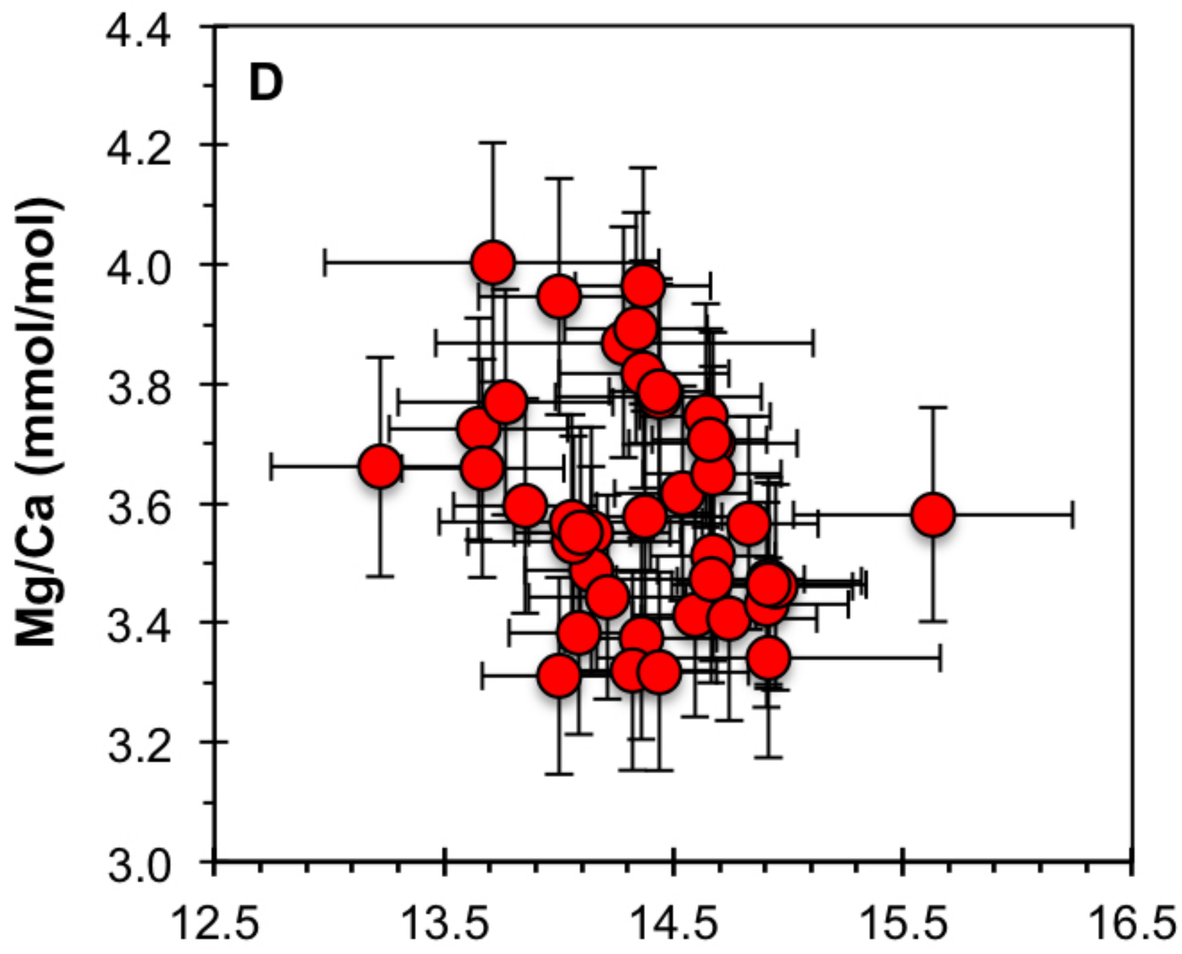
D
Mg/Ca (mmol/mol)
4.4
4.2
4.0
3.8
3.6
3.4
3.2
3.0
12.5
13.5
14.5
15.5
16.5
δ11B (‰)

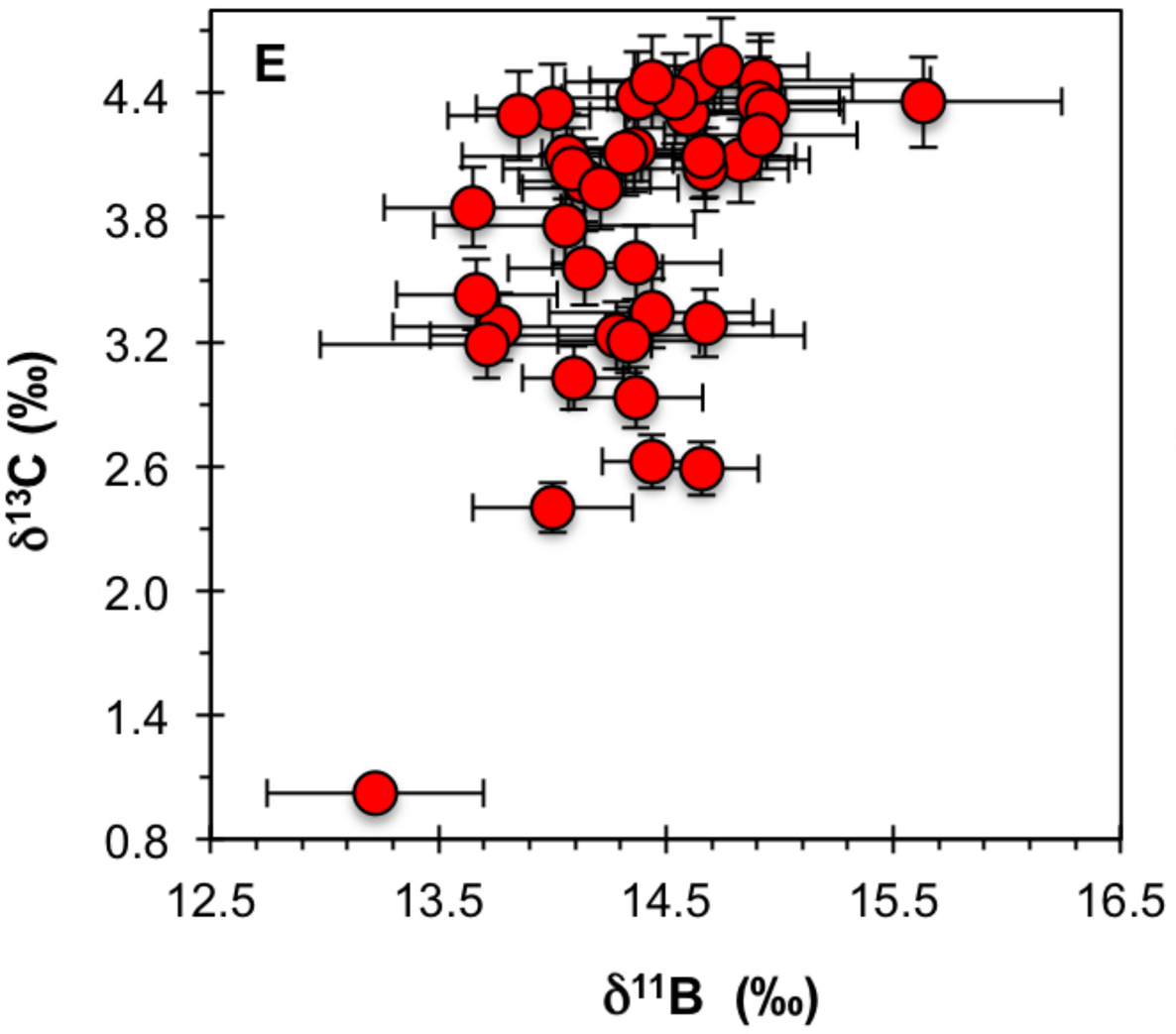
E
δ13C (‰)
4.4
3.8
3.2
2.6
2.0
1.4
0.8
12.5
13.5
14.5
15.5
16.5
δ11B (‰)

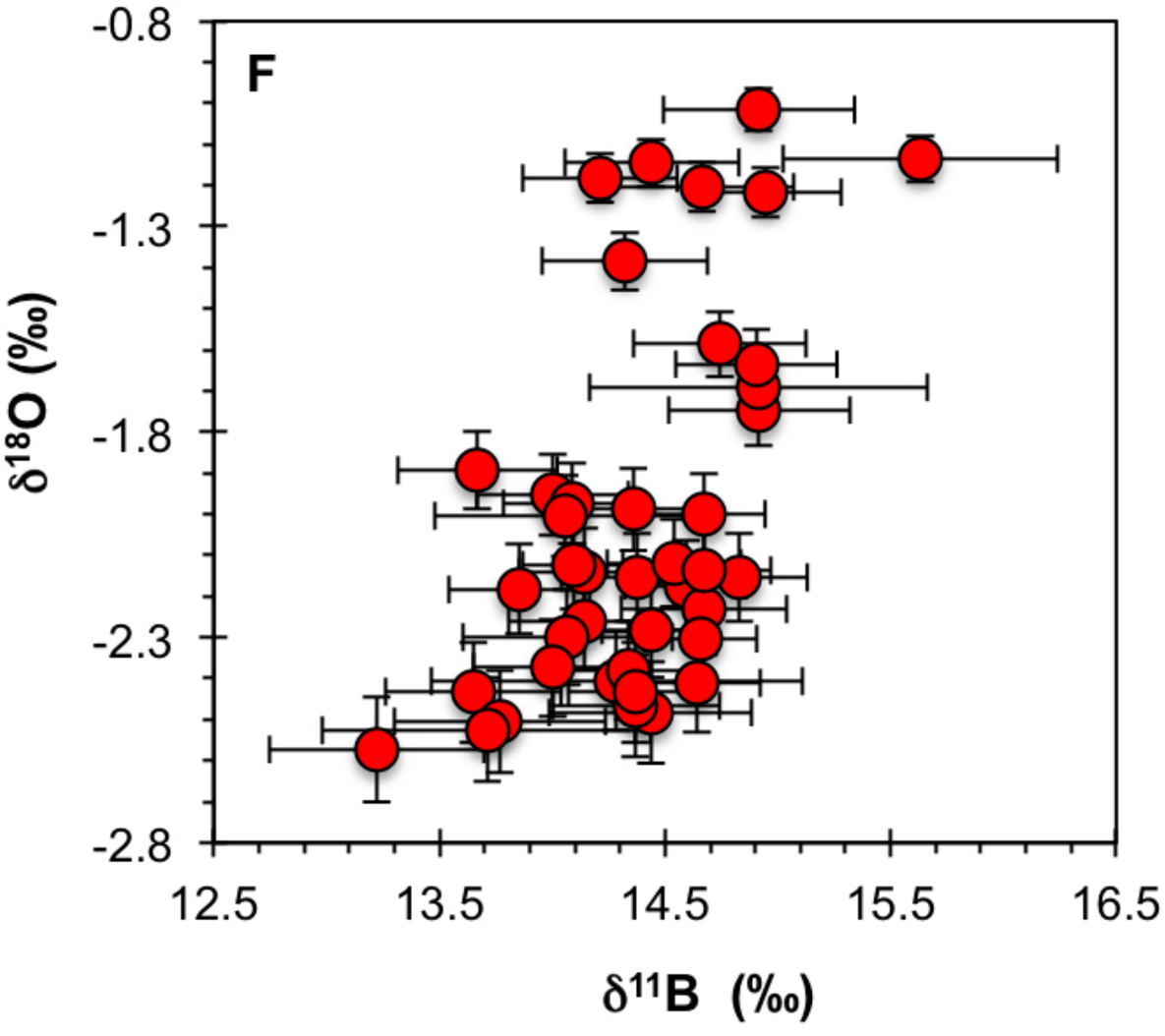
F
δ18O (‰)
-0.8
-1.3
-1.8
-2.3
-2.8
12.5
13.5
14.5
15.5
16.5
δ11B (‰)

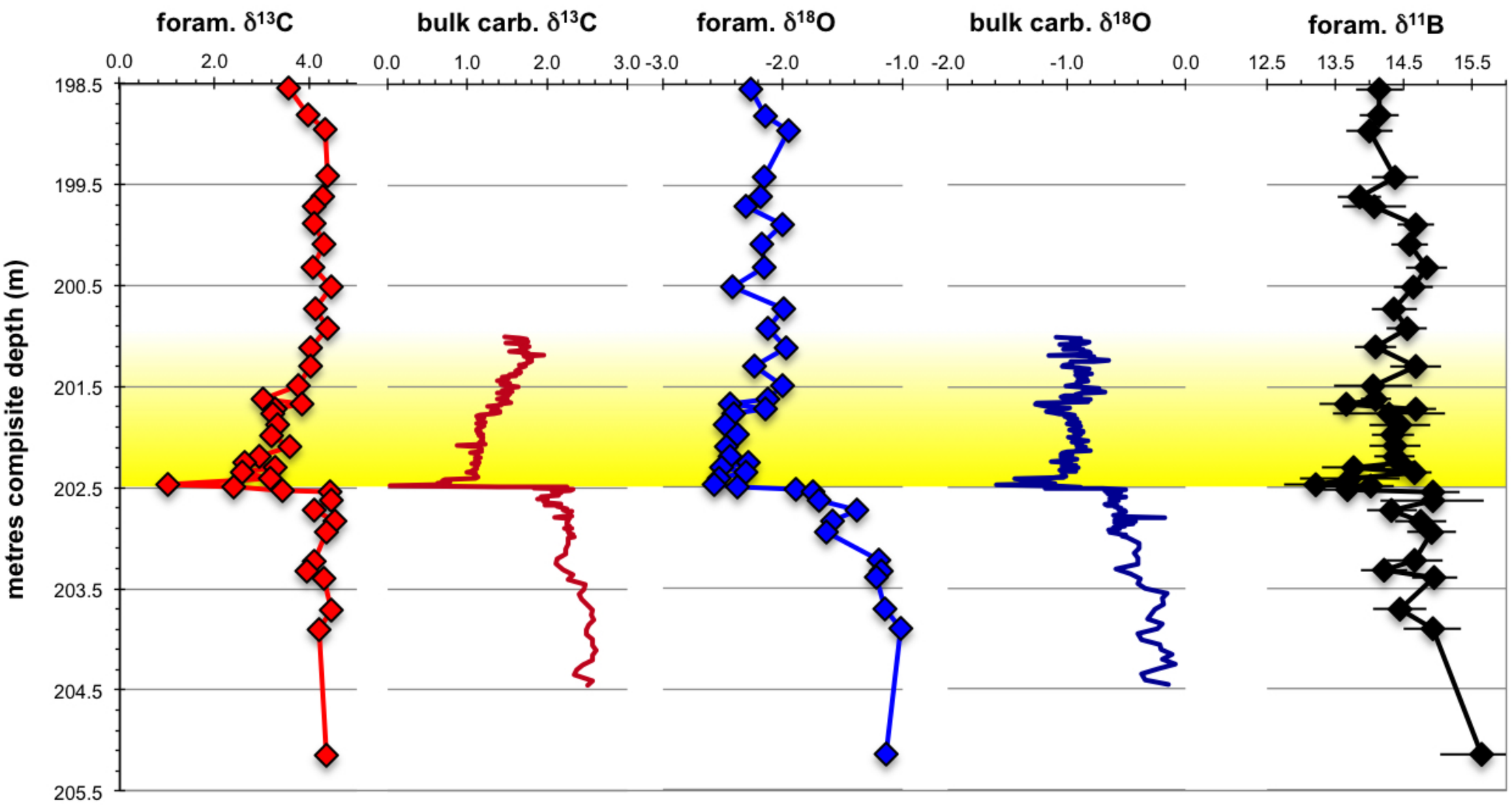
foram. δ13C
bulk carb. δ13C
foram. δ18O
bulk carb. δ18O
foram. δ11B
0.0
2.0
4.0
0.0
1.0
2.0
3.0
-3.0
-2.0
-1.0
-2.0
-1.0
0.0
12.5
13.5
14.5
15.5
198.5
199.5
200.5
201.5
202.5
203.5
204.5
205.5
metres compisite depth (m)

A

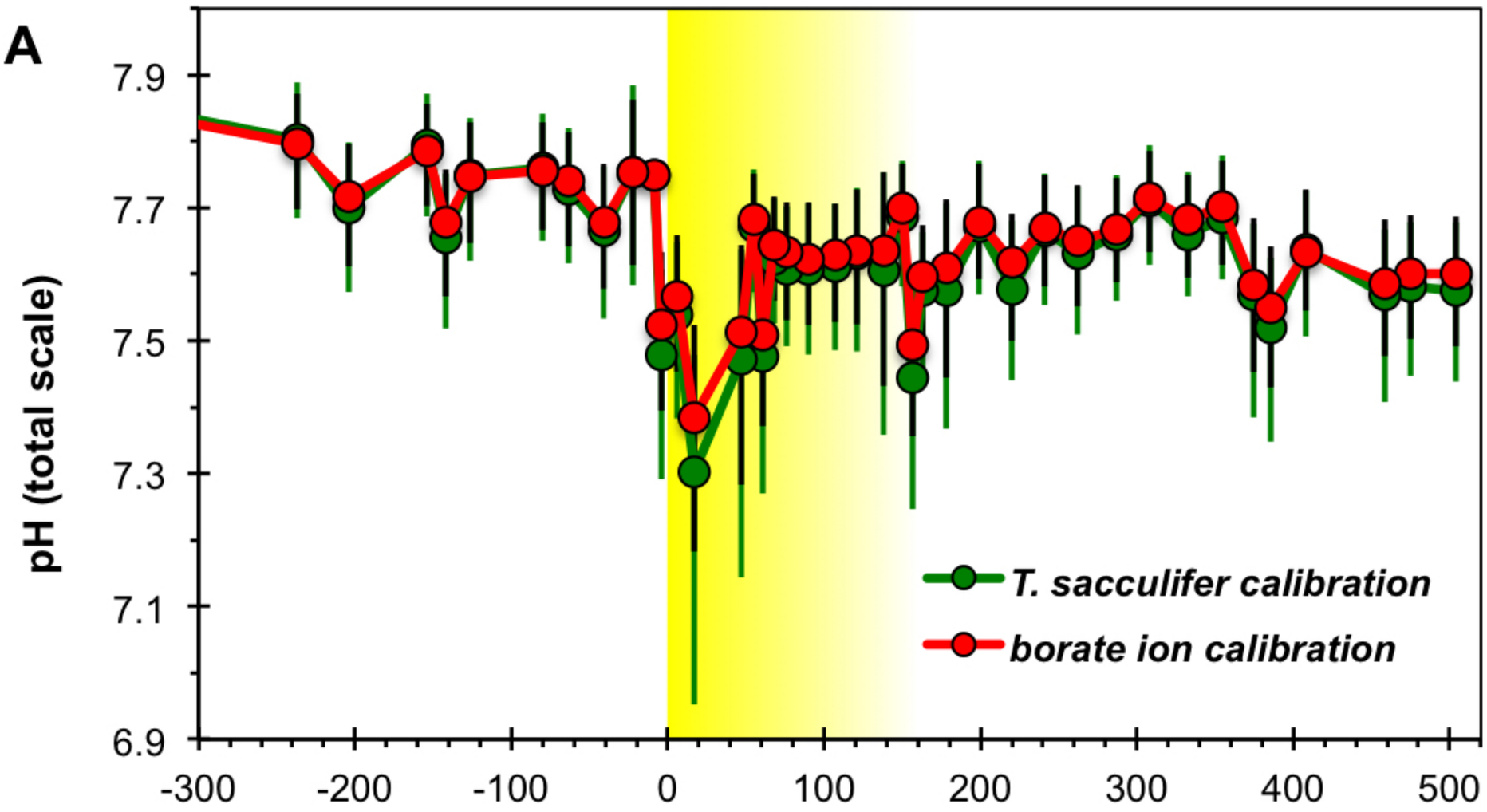
pH (total scale)
7.9
7.7
7.5
7.3
7.1
6.9
-300
-200
-100
0
100
200
300
400
500
time relative to CIE (ka)
T. sacculifer calibration
borate ion calibration

B

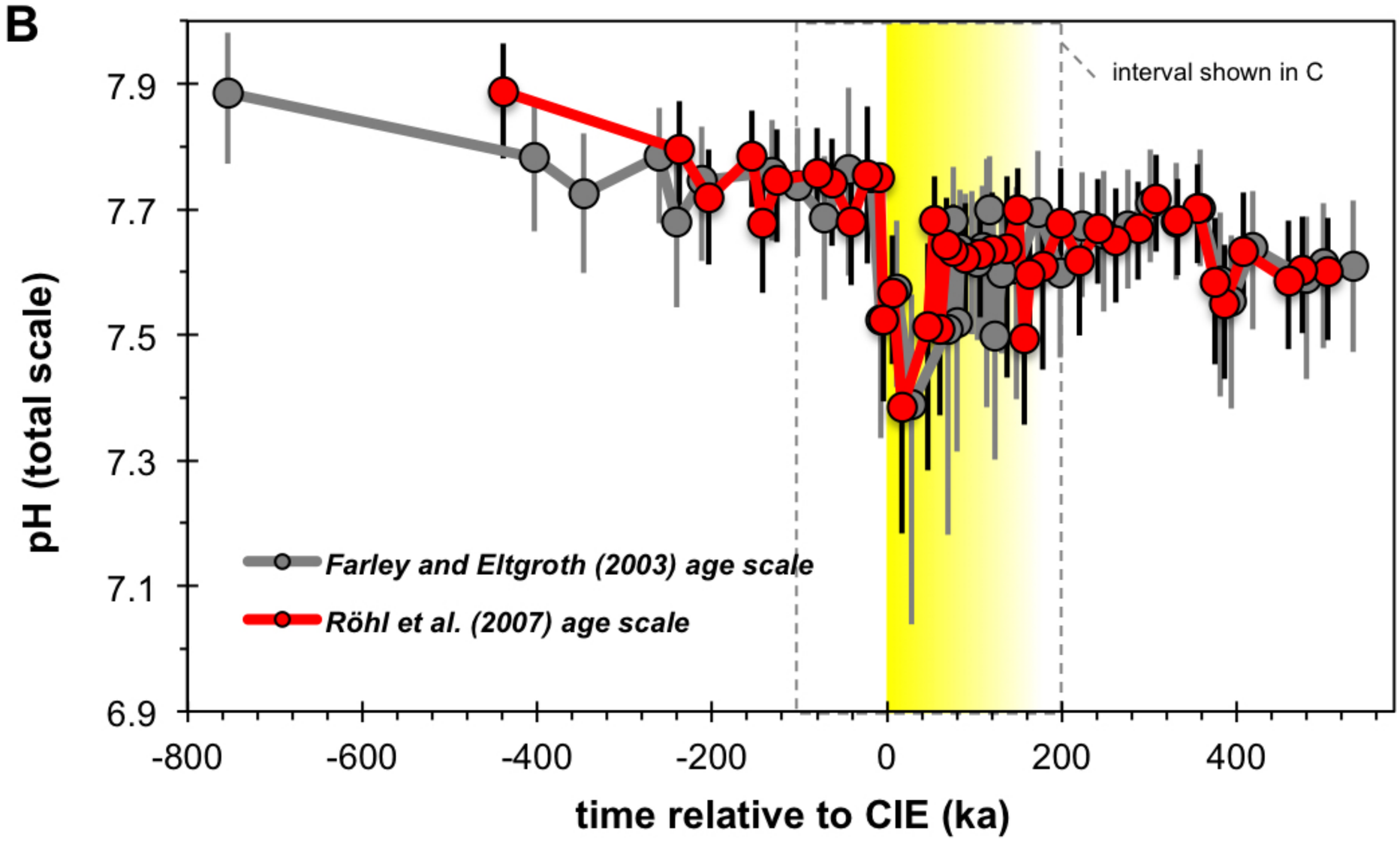
pH (total scale)
7.9
7.7
7.5
7.3
7.1
6.9
-800
-600
-400
-200
0
200
400
time relative to CIE (ka)
interval shown in C
Farley and Eltgroth (2003) age scale
Röhl et al. (2007) age scale

C

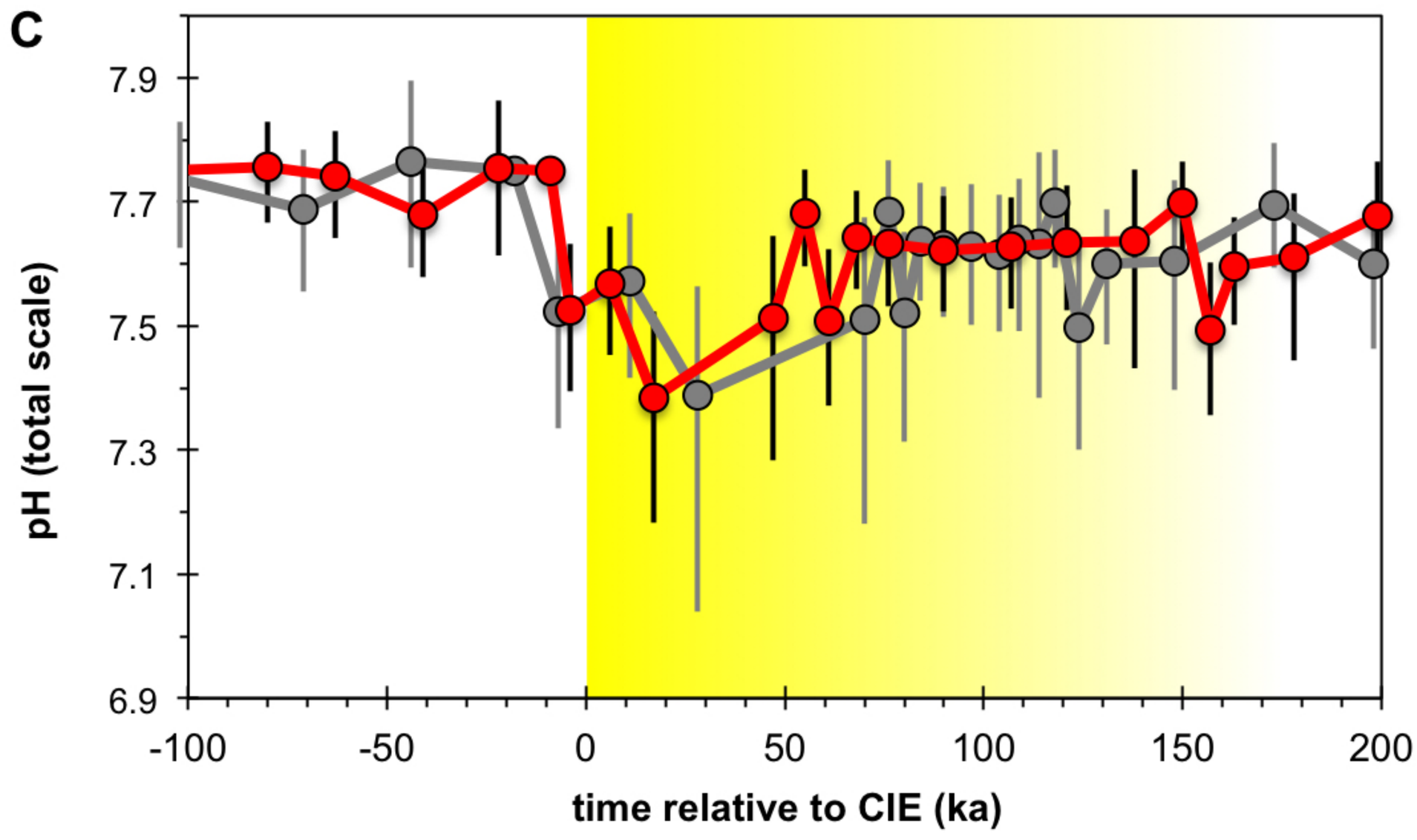
pH (total scale)
7.9
7.7
7.5
7.3
7.1
6.9
-100
-50
0
50
100
150
200
time relative to CIE (ka)

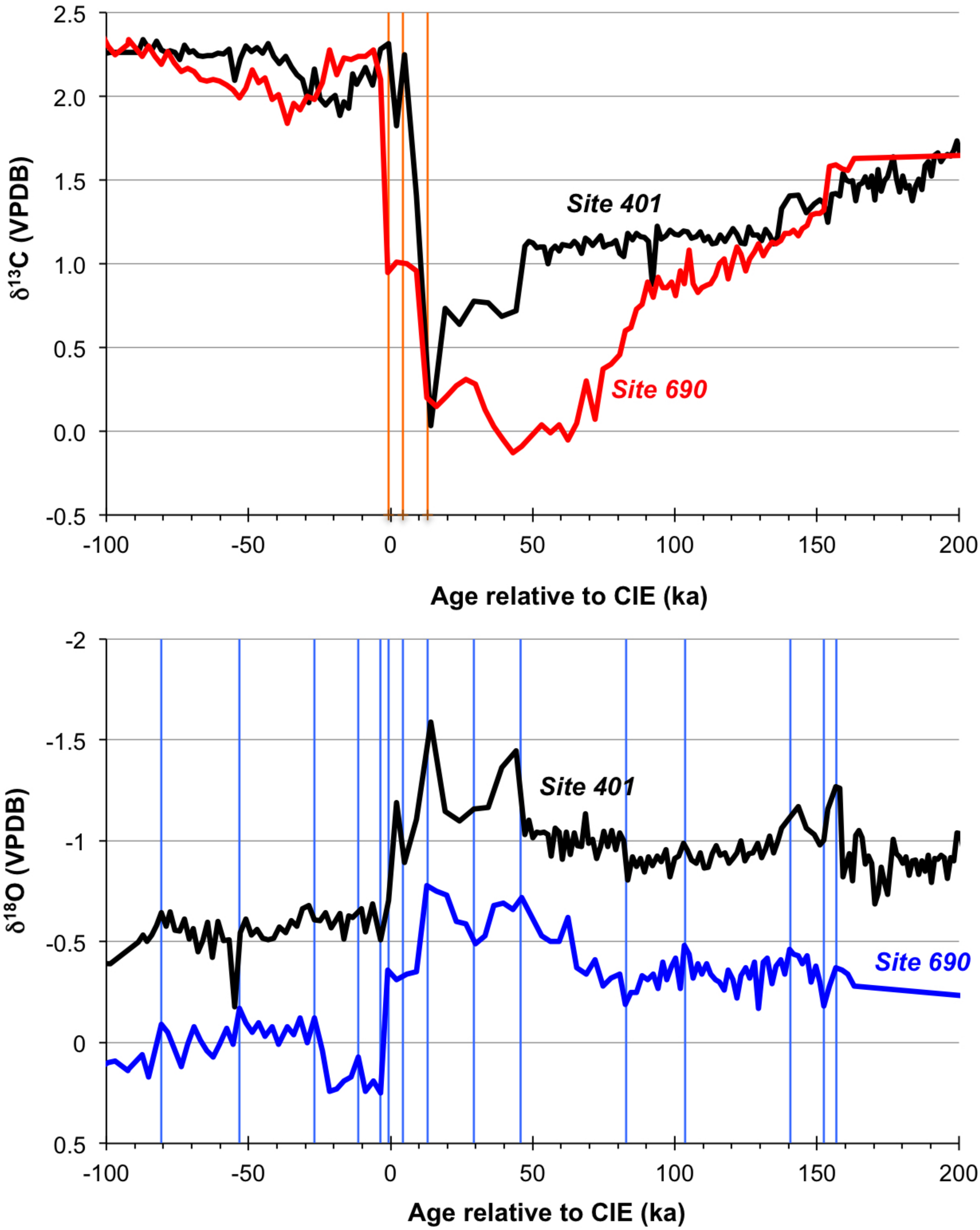
2.5
2.0
1.5
1.0
0.5
0.0
-0.5
δ13C (VPDB)
Site 401
Site 690
-100
-50
0
50
100
150
200
Age relative to CIE (ka)
-2
-1.5
-1
-0.5
0
0.5
δ18O (VPDB)
Site 401
Site 690
-100
-50
0
50
100
150
200
Age relative to CIE (ka)

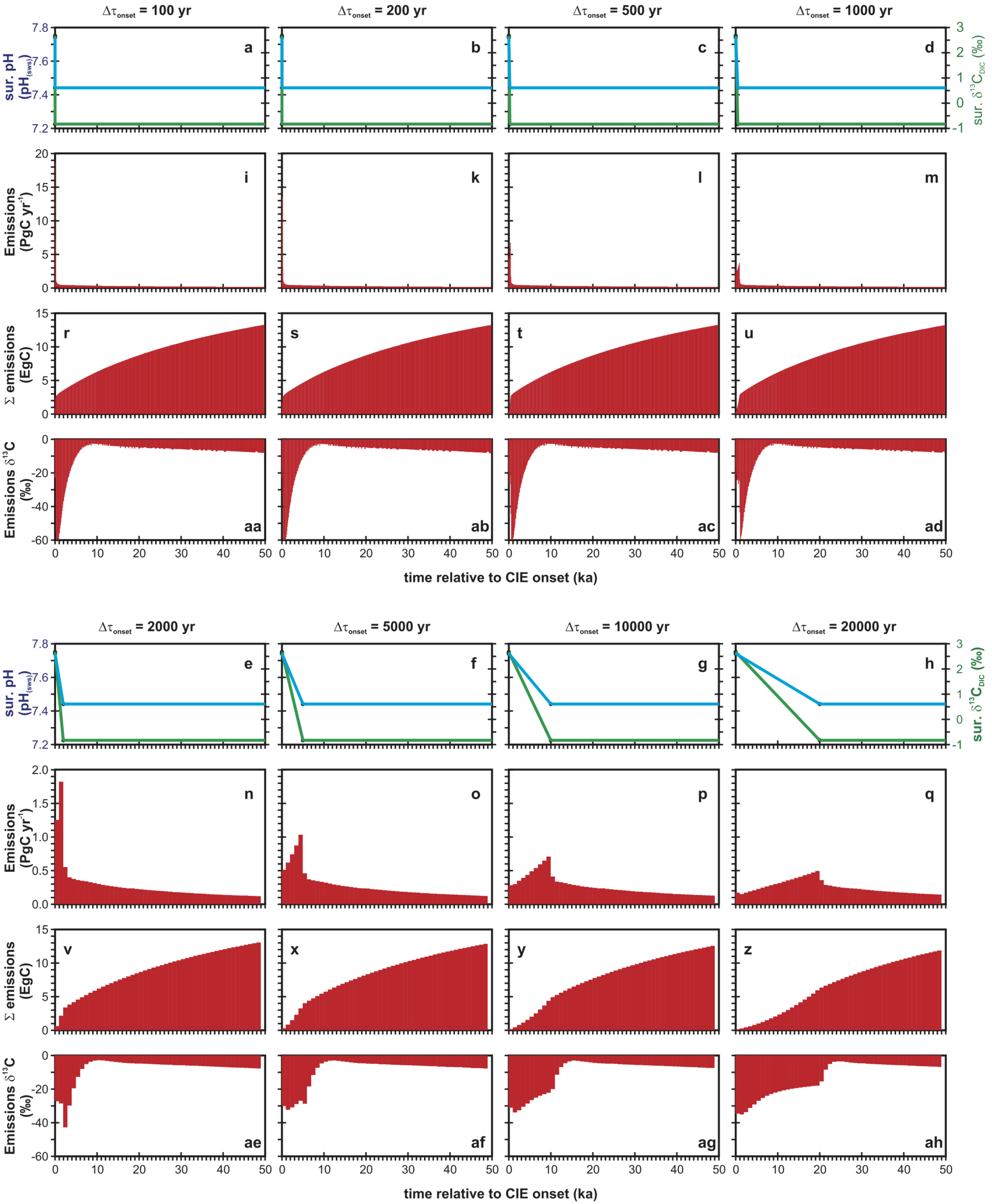
Δτonset = 100 yr
Δτonset = 200 yr
Δτonset = 500 yr
Δτonset = 1000 yr
sur. pH (pH(sws))
sur. δ13CDIC (‰)
Emissions (PgC yr-1)
Σ emissions (EgC)
Emissions δ13C (‰)
a
b
c
d
i
k
l
m
r
s
t
u
aa
ab
ac
ad
time relative to CIE onset (ka)
Δτonset = 2000 yr
Δτonset = 5000 yr
Δτonset = 10000 yr
Δτonset = 20000 yr
e
f
g
h
n
o
p
q
v
x
y
z
ae
af
ag
ah

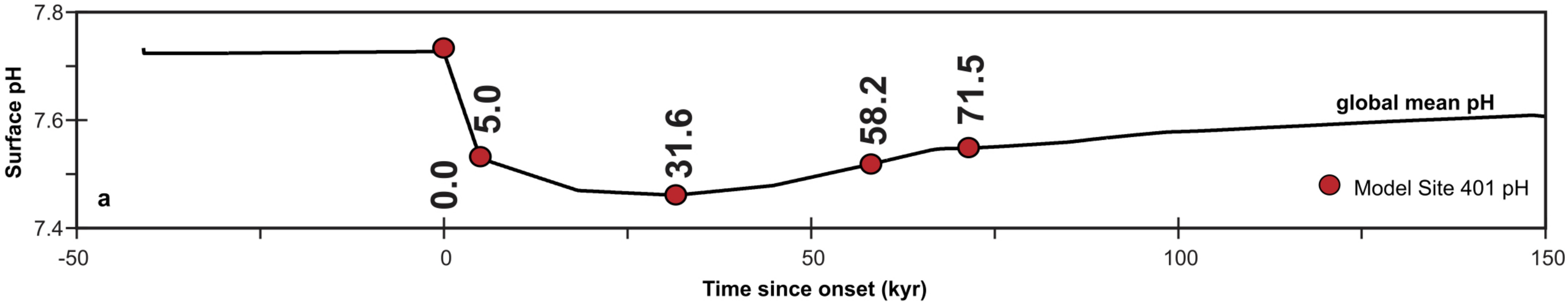

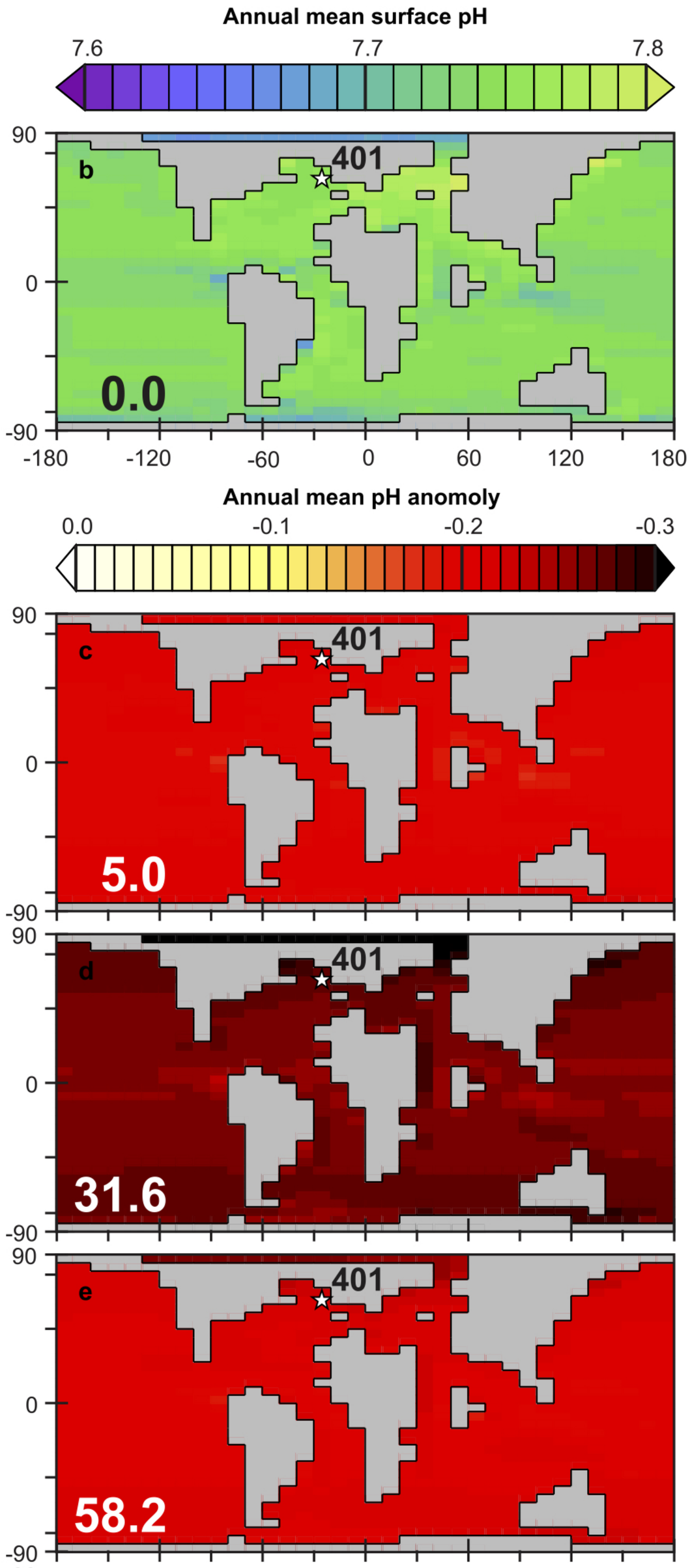

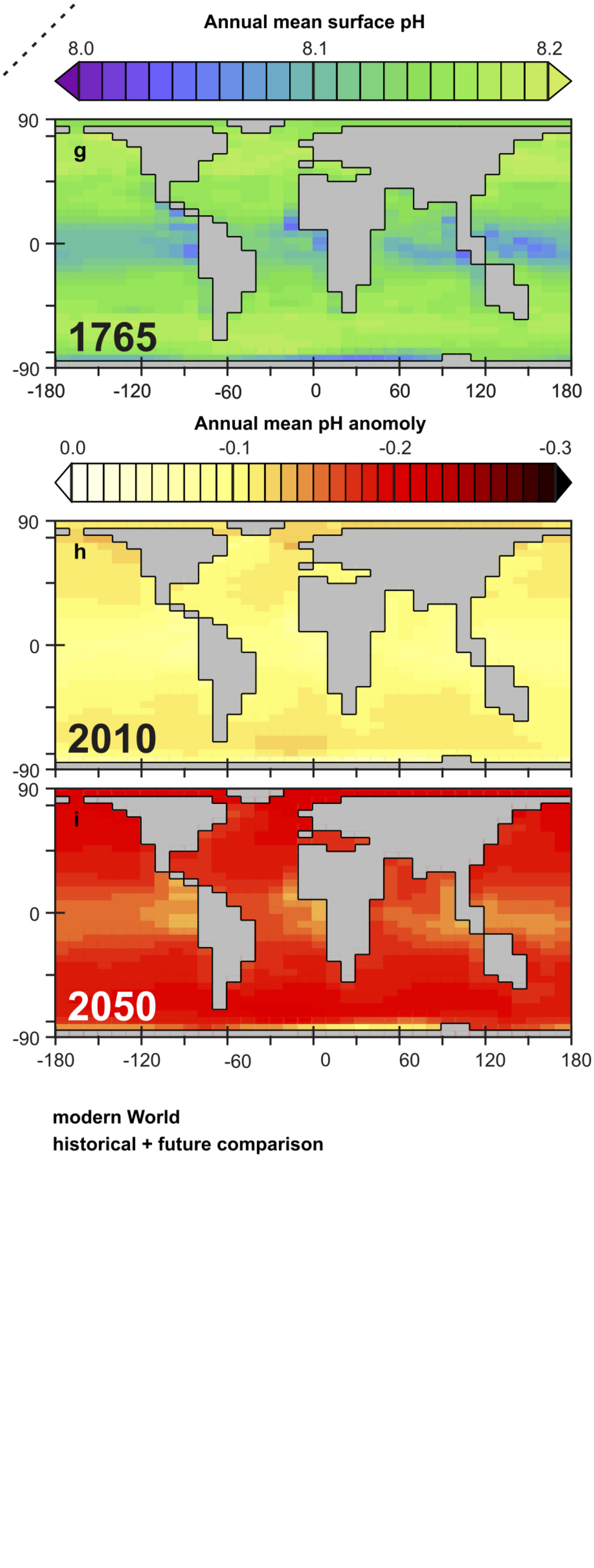

modern World
historical + future comparison

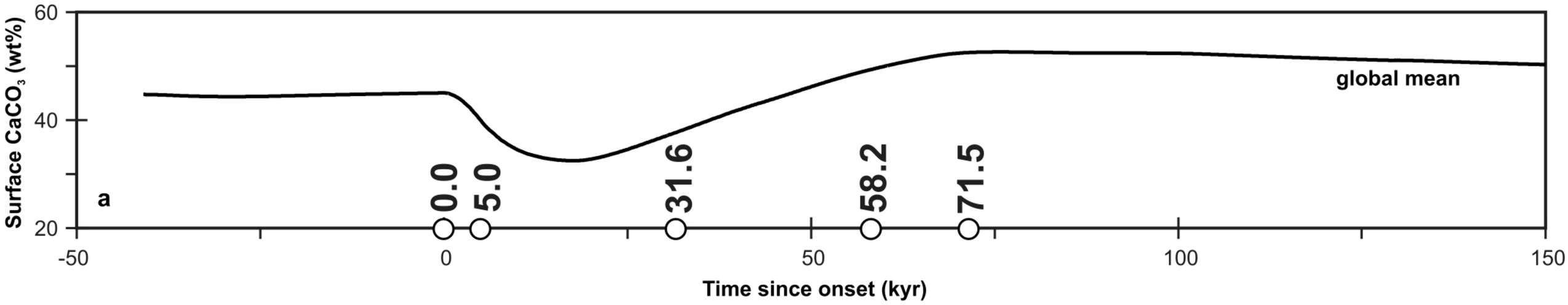
Surface CaCO3 (wt%)
60
40
20
a
global mean
0.0
5.0
31.6
58.2
71.5
-50
0
50
100
150
Time since onset (kyr)

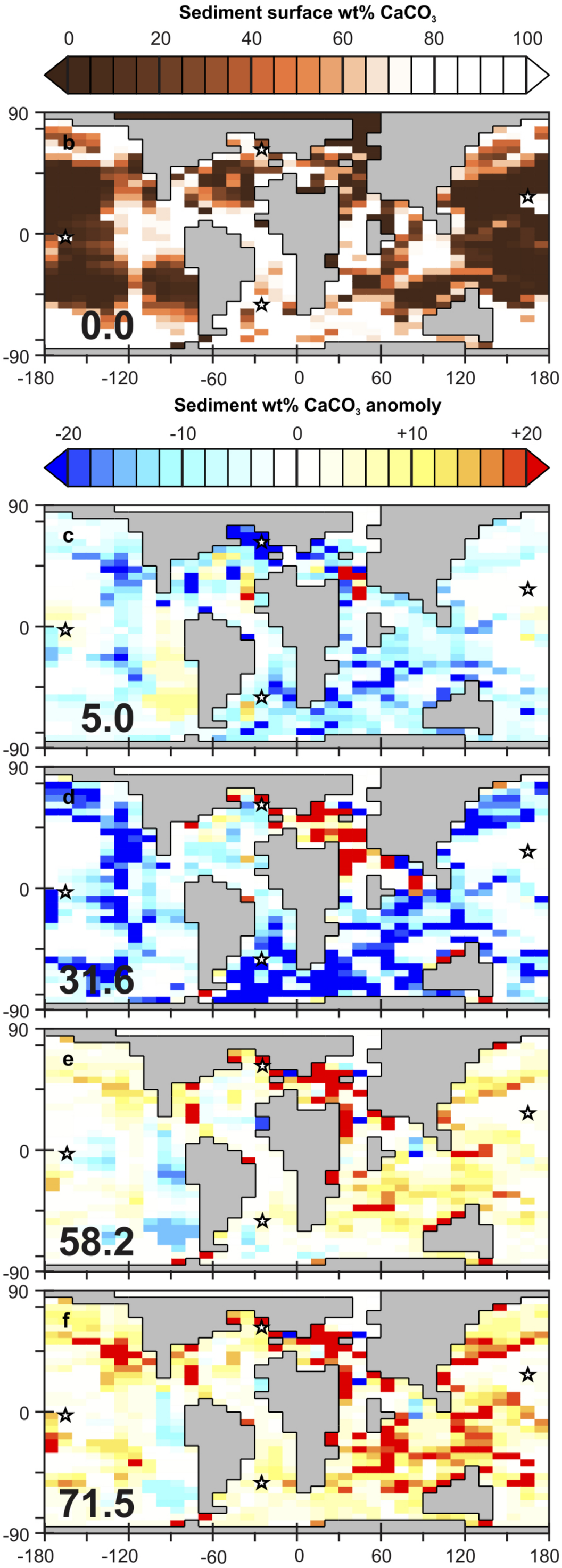
Sediment surface wt% CaCO3
0
20
40
60
80
100
b
0.0
Sediment wt% CaCO3 anomoly
-20
-10
0
+10
+20
c
5.0
d
31.6
e
58.2
f
71.5
90
0
-90
-180
-120
-60
0
60
120
180

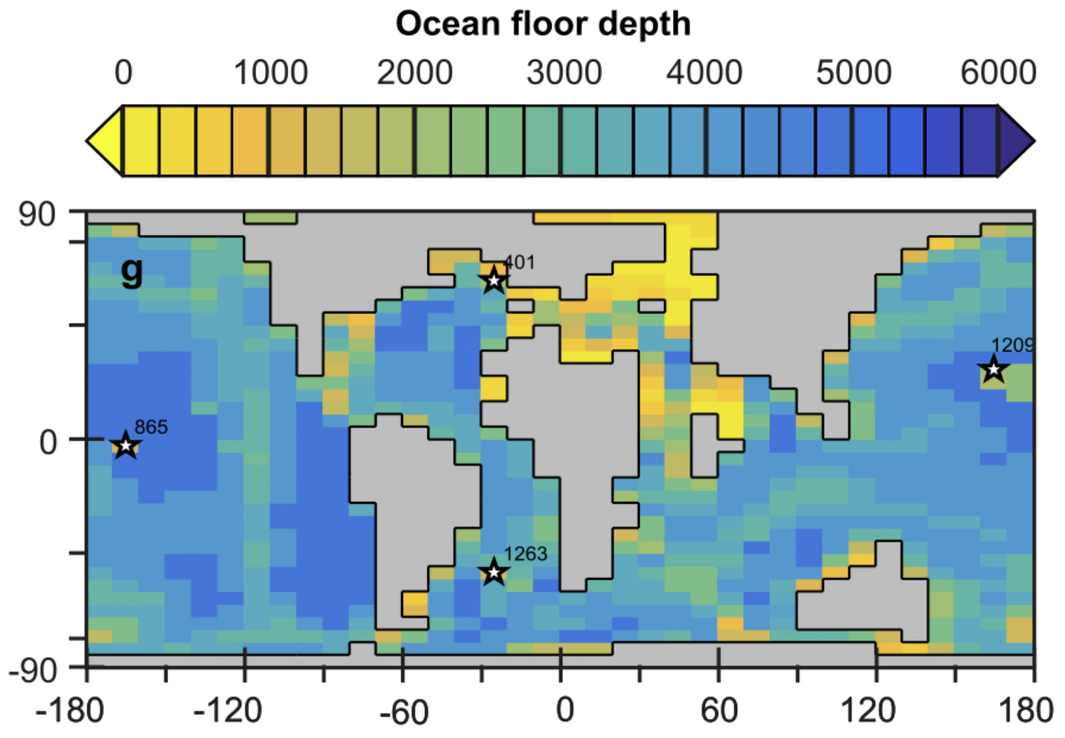
Ocean floor depth
0
1000
2000
3000
4000
5000
6000
g
401
1209
865
1263
90
0
-90
-180
-120
-60
0
60
120
180

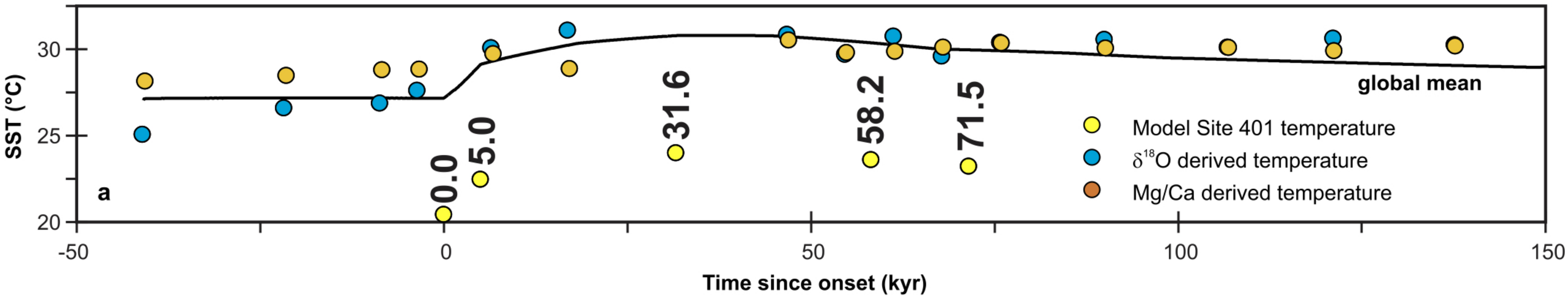
SST (°C)
30
25
20
a
0.0
5.0
31.6
58.2
71.5
global mean
Model Site 401 temperature
δ18O derived temperature
Mg/Ca derived temperature
-50
0
50
100
150
Time since onset (kyr)

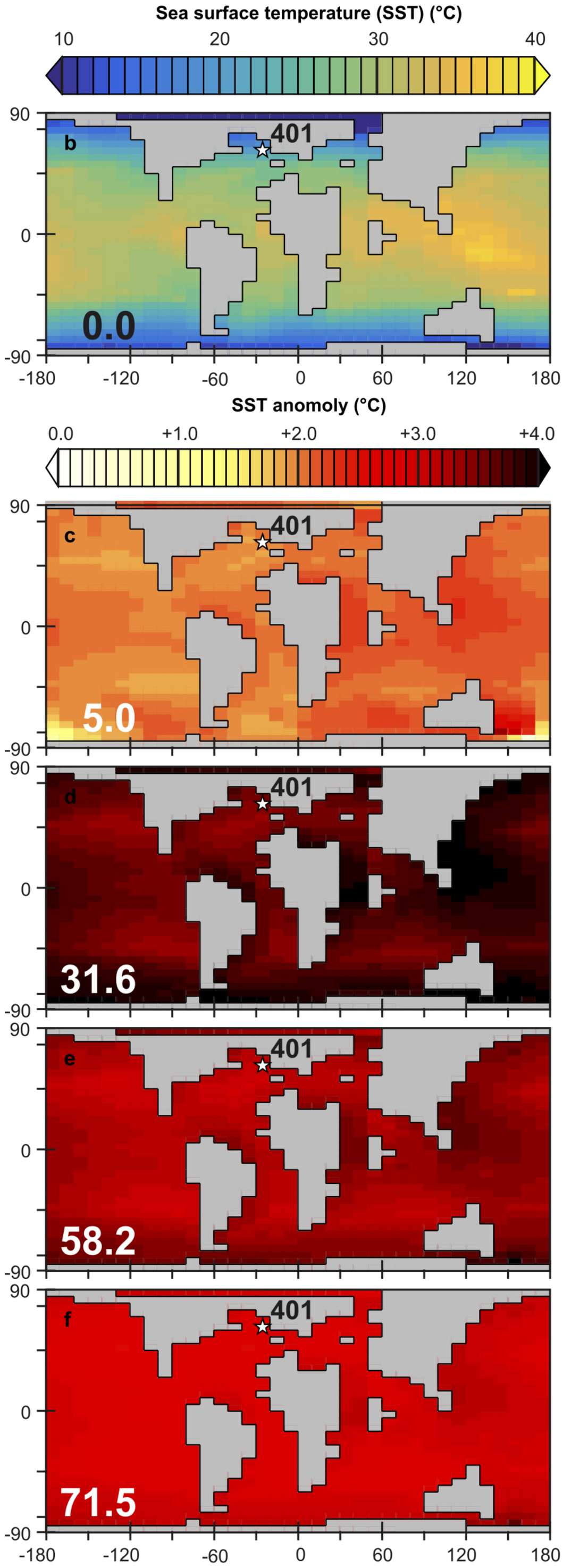
Sea surface temperature (SST) (°C)
10
20
30
40
90
0
-90
b
401
0.0
-180
-120
-60
0
60
120
180
SST anomoly (°C)
0.0
+1.0
+2.0
+3.0
+4.0
c
5.0
d
31.6
e
58.2
f
71.5

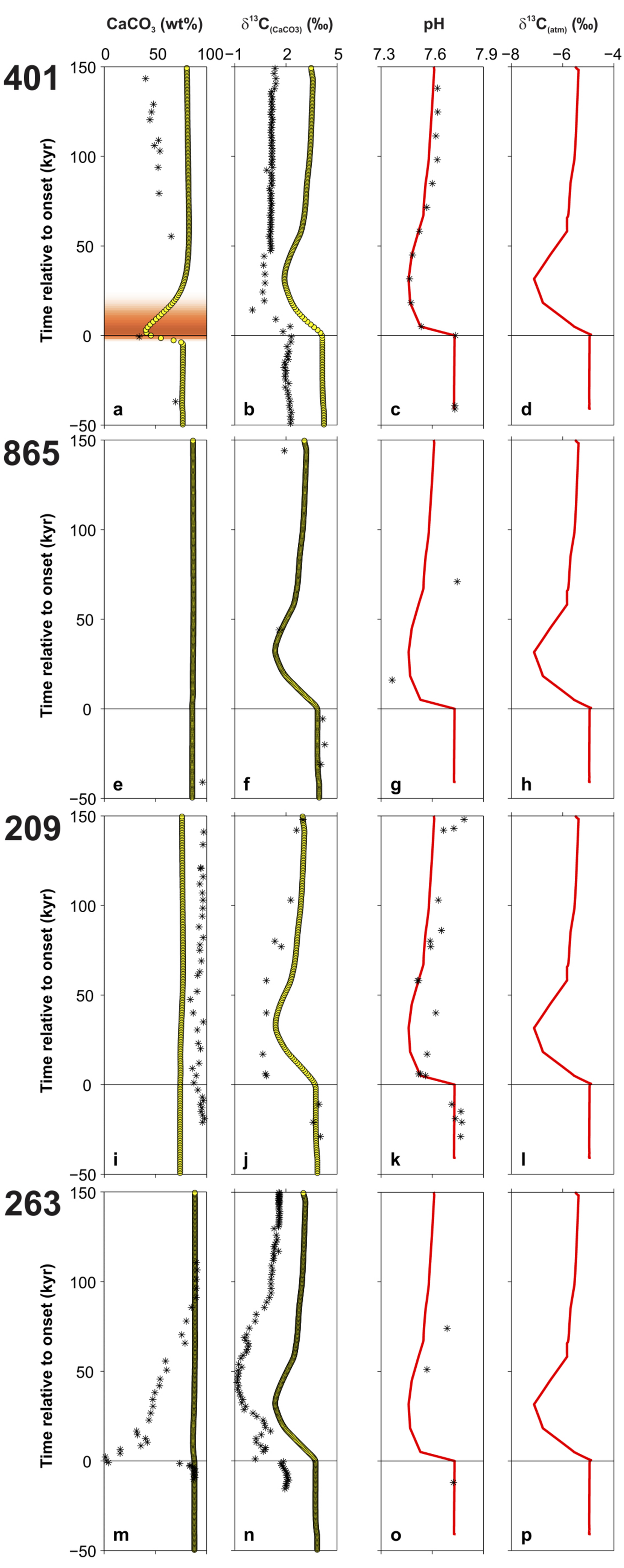
401
865
1209
1263
CaCO3 (wt%)
δ13C(CaCO3) (‰)
pH
δ13C(atm) (‰)
Time relative to onset (kyr)
150
100
50
0
−50
0
50
100
−1
2
5
7.3
7.6
7.9
−8
−6
−4
a
b
c
d
e
f
g
h
i
j
k
l
m
n
o
p

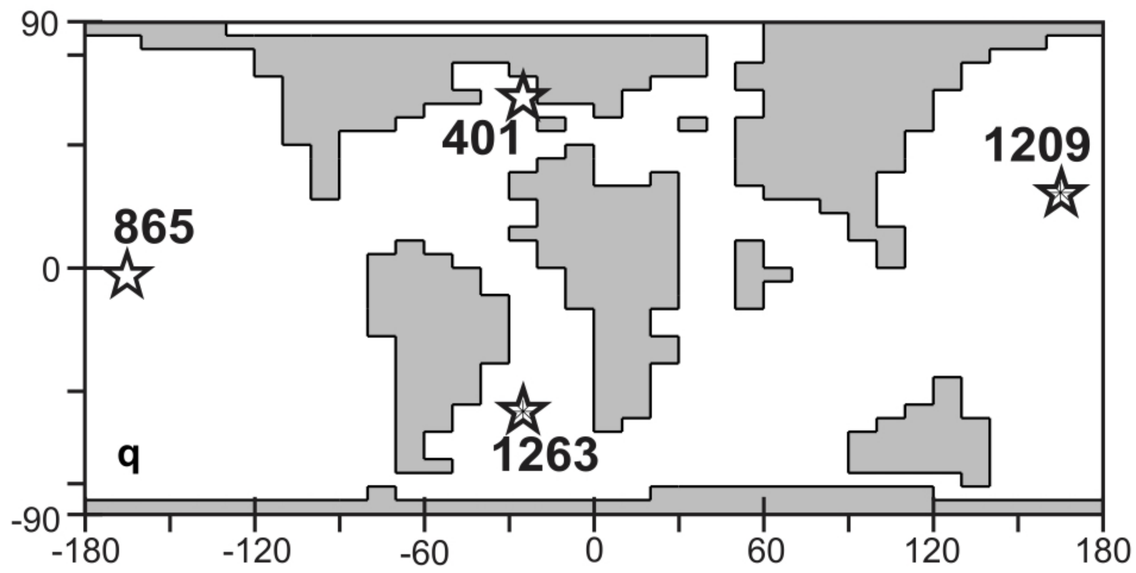
401
1209
865
1263
q
90
0
-90
-180
-120
-60
0
60
120
180

a

Experiment ID	experimental assumptions					peak emissions	cumulative emissions		cumulative C_{org} burial		ΔSST	peak excess weathering
	age model	$\delta^{11}B$ envelope	smoothed data?	weathering?	Corg burial?	(PgC yr^{-1})	total (PgC)	mean $\delta^{13}C$ (‰)	total (PgC)	mean $\delta^{13}C$ (‰)	(°C)	(PgC yr^{-1})
R07sm_HI	**R07**	**high**	**YES**	**YES**	**NO**	**0.41**	**5,688**	**-18.9**	**---**	**---**	**2.25**	**0.030**
R07sm	**R07**	**mean**	**YES**	**YES**	**NO**	**0.58**	**10,213**	**-11.1**	**---**	**---**	**3.64**	**0.053**
R07sm_LO	**R07**	**low**	**YES**	**YES**	**NO**	**1.16**	**19,964**	**-6.6**	**---**	**---**	**5.99**	**0.105**
FEsm_HI	FE	high	YES	YES	NO	0.17	6,502	-16.5	---	---	2.10	0.038
FEsm	FE	mean	YES	YES	NO	0.36	12,020	-9.8	---	---	3.09	0.069
FEsm_LO	FE	low	YES	YES	NO	0.64	24,124	-6.0	---	---	4.80	0.132
R07rw	**R07**	**mean**	**NO**	**YES**	**NO**	**0.61**	**10,984**	**-12.1**	**---**	**---**	**4.07**	**0.061**
FErw	FE	mean	NO	YES	NO	0.45	12,749	-10.2	---	---	3.14	0.072
R07sm_noW	**R07**	**mean**	**YES**	**NO**	**NO**	**0.52**	**6,407**	**-16.7**	**---**	**---**	**3.34**	**---**
FEsm_noW	FE	mean	YES	NO	NO	0.30	6,665	-16.4	---	---	2.72	---
R07sm_HI_Corg	**R07**	**high**	**YES**	**YES**	**YES**	**0.41**	**7,670**	**-18.0**	**2,607**	**-30.0**	**2.25**	**0.030**
R07sm_Corg	**R07**	**mean**	**YES**	**YES**	**YES**	**0.58**	**12,220**	**-10.9**	**2,540**	**-30.5**	**3.64**	**0.053**
R07sm_LO_Corg	**R07**	**low**	**YES**	**YES**	**YES**	**1.16**	**22,593**	**-7.1**	**3,333**	**-30.9**	**5.99**	**0.105**

b

Duration of onset (yr)	peak emissions (PgC yr^{-1})	cumulative emissions over onset		cumulative emissions @ 20,000 yr		cumulative emissions @ 50,000 yr	
		total (PgC)	mean $\delta^{13}C$ (‰)	total (PgC)	mean $\delta^{13}C$ (‰)	total (PgC)	mean $\delta^{13}C$ (‰)
100	20.00	1,897	-19.0	8,695	-17.0	13,256	-13.4
200	15.21	2,355	-18.4	8,688	-17.0	13,252	-13.4
500	6.90	2,588	-21.5	8,664	-17.0	13,239	-13.6
1,000	3.72	2,799	-24.5	8,613	-17.1	13,200	-13.4
2,000	2.08	3,074	-27.6	8,526	-17.2	13,181	-13.4
5,000	1.07	3,751	-29.0	8,202	-17.8	13,007	-13.5
10,000	0.70	4,691	-26.3	7,612	-18.8	12,706	-13.6
20,000	0.48	6,141	-22.0	6,141	-22.0	12,025	-14.0

SI Guide for

Very large release of mostly volcanic carbon during the Paleocene-Eocene Thermal Maximum

By

Marcus Gutjahr[1,2*], Andy Ridgwell[3,4], Philip F. Sexton[5], Eleni Anagnostou[1], Paul N. Pearson[6], Heiko Pälike[7], Richard D. Norris[8], Ellen Thomas[9,10] and Gavin L. Foster[1]

The following supplementary files accompany the main publication:

1) Supplementary Information SI1 containing a detailed account on Earth System Modelling approaches used as a pdf file.
2) Supplementary Table S1 containing foraminifera-based stable isotope results, relative sample ages, selected elemental ratios as well as calculated mixed layer pH (as a Microsoft Excel file).
3) Supplementary Table S2 containing bulk carbonate stable carbon and oxygen isotope results, also presented alongside relative ages following our two alternative age models (see Methods) (as a Microsoft Excel file).

SUPPLEMENTARY INFORMATION S1

Very large release of mostly volcanic carbon during the Paleocene-Eocene Thermal Maximum

By

Marcus Gutjahr[1,2*], Andy Ridgwell[3,4], Philip F. Sexton[5], Eleni Anagnostou[1], Paul N. Pearson[6], Heiko Pälike[7], Richard D. Norris[8], Ellen Thomas[9,10] and Gavin L. Foster[1]

[1] Ocean and Earth Science, National Oceanography Centre Southampton, University of Southampton, UK

[2] GEOMAR Helmholtz Centre for Ocean Research Kiel, Germany mgutjahr@geomar.de

(* corresponding author)

[3] School of Geographical Sciences, Bristol University, Bristol, UK

[4] Department of Earth Sciences, University of California-Riverside, Riverside, CA, USA

[5] School of Environment, Earth & Ecosystem Sciences, The Open University, Milton Keynes, UK

[6] School of Earth and Ocean Sciences, Cardiff University, Cardiff, UK

[7] MARUM, Center for Marine Environmental Sciences, University of Bremen, Germany

[8] Scripps Institution of Oceanography, University of California, San Diego, La Jolla, U.S.A.

[9] Department of Geology and Geophysics, Yale University, New Haven CT, U.S.A.

[10] Department of Earth and Environmental sciences, Wesleyan University, Middletown CT, USA

Earth system modelling – further model and model-data analysis

In our main analysis, we noted that the predicted peak increase in global surface temperature is close to estimates derived from compilations of available proxy records, while our inferred source and total emissions of carbon falls within existing estimates of volcanic and/or volcanic driven activity and carbon release adding plausibility to our inferences. We furthermore noted that none of: uncertainties in the age model, uncertainties in the boron proxy pH reconstruction, or whether assimilation is carried out on smoothed vs. 'raw' data, unduly affect our conclusions. In this section, we greatly extend the scope of model-data assessment to span a range of sites and proxies in order to provide a more in-depth and independent test of our preferred model-generated scenario of PETM carbon release as well as elucidate model uncertainties.

Our primary data assimilated in the model is the reconstructed ocean surface pH at Site 401, and this leads directly to our reconstruction of total carbon release via determination of the source isotopic composition of this carbon. To date, four deep ocean sites exist for which pH has been reconstructed by means of boron isotopes (shown in Fig. 2) – 401, 865, 1209, and 1263. Comparison of the model-projected evolution of surface ocean pH for each of the four locations vs. the data reconstructions, is shown in Extended Data Fig. 9 (and see Extended Data Fig. 6). To this comparison we also add model-projected (also for experiment ID 'R07sm_Corg') vs. observed evolution of sedimentary carbonate ($CaCO_3$) content (e.g. Extended Data Fig. 7), as this relates to (but does not directly reflect) carbon emissions, plus a comparison of modelled and observed bulk carbonate $\delta^{13}C$ for completeness.

For Site 401, the model matches the observed pH (excepting a small deviation during PETM recovery), but as this data is assimilated in the model, this is expected. The available observed wt% $CaCO_3$ data at Site 401 is patchy, but from what exists spanning pre-event to peak event, the model projected evolution of wt% $CaCO_3$ closely matches the data. However, during PETM recovery when the model predicts (and one would *a priori* expect) a prolonged overshoot in wt% $CaCO_3$, the data exhibits an unexpected decline to below pre-event values, not reproduced by the model. One possible explanation is that evidence for an increase in the hydrological cycle following peak warming of the PETM drove increased input of terrestrial (clay) materials (not accounted for in the model simulation), thereby diluting the carbonate

content in the upper part of the early Eocene section at Site 401[1]. Lastly, the model parallels (with an offset) the bulk carbonate $\delta^{13}C$ response except during the recovery, which the bulk $CaCO_3$ $\delta^{13}C$ does not appear to record (potentially also related to a higher clay input to the depositional site[1]). Note that monospecific planktic foraminiferal $\delta^{13}C$ data was assimilated in the model as reflecting surface ocean geochemistry. In contrast, the bulk observed and modelled records in this analysis, also reflect sedimentary preservation and plankton assemblage effects.

For Site 865, pH data is extremely sparse and suggests that the model slightly underestimates the magnitude of the pH change (although taking into account the uncertainty in the data (Fig. 2), the model projection of the peak excursion value is consistent with the data) as well as the rapidity of its recovery. Only pre-event wt% $CaCO_3$ data is available, which the model closely reproduces at this site. For bulk $CaCO_3$ $\delta^{13}C$ – the model matches almost exactly the data across the onset and peak of the event given a very sparse sampling density, but slightly over-predicts the recovery in $\delta^{13}C$ as compared to the single available recovery interval data point.

For Site 1209, the model shows a visually very good correspondence with the pH data, except for two points during the peak which on face value suggest a partial recovery before renewal of low pH values. Again, in this simple comparative analysis we have not taken into account data uncertainty (plotted in Fig. 2) and much of the remaining model-data misfit can be account for by this uncertainty. Little response is seen in either the model or data with respect to wt% $CaCO_3$. For bulk carbonate $\delta^{13}C$, the modelled excursion is slightly smaller and lagged as compared to the data.

Finally, for Site 1263, the pH recovery is a little too slow in the model compared to the data (but again, this is without taking into account any data uncertainty) although what peak PETM conditions might have been are not resolved in the data. As per Site 1209, bulk carbonate $\delta^{13}C$ is lagged in the model and the excursion a little smaller than observed. However, there is a stark misfit with respect to the observed wt% $CaCO_3$ response across the event (discussed in detail below).

What can this analysis tell us about how confident we can be in the inferred emissions scenario and about model uncertainly in general? Firstly, there does not seem to be any systematic bias in the evolution of surface ocean pH in the model as compared to the data, with the exception that simulated pH recovery may be a little

too slow. The most likely explanation for this would be that the rate of carbon removal via silicate weathering and/or organic matter burial is being underestimated. While bulk $CaCO_3$ $\delta^{13}C$ records indicate that the model response is broadly consistent with observations, there is a tendency for the modelled excursion to be lagged and narrower than observed. This may simply reflect differences between the internal age model in the simulations, which assumes a constant detrital sedimentation rate (following *Jennions et al.*[2]) and the Site 690 tied age models applied to the four sites. Changes in the intensity and nature of bioturbation and in the assumptions of which fraction of $CaCO_3$ is being dissolved, may also play a role (see ref. 2 for a discussion of similar phenomena in respect to a subsequent hyperthermal event). The wt% $CaCO_3$ records are a little more revealing, particularly for Site 1263 and to a lesser extent, in the recovery at Site 401. While the deep sea faunal and hence bioturbation response may be important (see ref. 3), model-data misfits likely indicate changes occurring in the ventilation and ocean circulation patterns that are not being appropriately reproduced in the model. This does not necessarily imply a significant uncertainty then exists in the diagnosed total carbon release across the PETM because of the relatively good model-data correspondence in pH – a surface property unlikely significantly impacted by changes in interior ocean ventilation patterns. Considerably more detailed and spatially resolved model-data analysis of the evolving patterns of carbonate preservation and burial would be needed to fully elucidate and quantify the implications of model biases in this respect (hence falling beyond the scope of this present study).

We can also look at how sedimentary carbonate content evolves in another way. Extended Data Fig. 7 shows the pre-event pattern of the $CaCO_3$ content of surface sediments together with a series of anomalies in wt% $CaCO_3$, using the same time-points as for the surface ocean pH analysis (Extended Data Fig. 6) (and still focussing on experiment ID 'R07sm_Corg'). We find an initial decline in wt% $CaCO_3$, reaching a nadir around 15-20 kyr after PETM onset. Mean global carbonate content then recovers and over-shoots (recorded in the 58.2 and 71.5 ka time-slices). Although the full spatial extent of $CaCO_3$ dissolution is not captured in the spatial snap-shots, our modelling indicates an early impact in the North Atlantic and Tethys, followed by an early recovery in those regions. In contrast, the full dissolution impact in the Pacific, Southern Atlantic, and Indian Oceans takes longer to develop and is

apparently more intense. Out of the latter three regions, reduced sedimentary carbonate content is greatest and most widespread in the Southern Atlantic and Indian Oceans as expected (e.g. Zeebe and Zachos[4]). We note that in the South Atlantic Ocean and in the vicinity of Walvis Ridge, enhanced carbonate dissolution is widespread, except at shallower depths such as the location of Site 1263. It should be noted that the bathymetry shown in Extended Data Fig. 7g and used for calculating the solubility of $CaCO_3$, deviates from the ocean circulation model bathymetry at the model locations of key deep-sea drilling sites, to facilitate model-data comparison. This is apparent in the existence of a 'plateau' at Shatsky Rise, and somewhat also at Walvis Ridge. Hence the partial model-data failure apparent in Figure Extended Data Fig. 9 may primarily reflect a model failure to correctly project intermediate water mass changes and characteristics (e.g. see *Jennions et al.*[2]), rather than a failure to account for carbonate dissolution and buffering in the deep South Atlantic as a whole.

Earth system modelling – uncertainty in projections

As in all numerical modelling and particularly for time-periods outside of the observational era, uncertainties in model projections exist and need to be recognized. These uncertainties can be minimized, as we have done here, by enforcing traceability to observed modern climatology and carbon cycling dynamics:

1. Employing a representation of ocean circulation and climate feedback calibrated and assessed against modern observational data[5,6], and making the minimal possible changes for the late Paleocene, namely: adjusted continental configuration and bathymetry, adjusted wind stress and wind speed, adjusted planetary albedo, reduced solar constant[7].
2. Employing a representation of ocean carbon, nutrient (here: just phosphate), and carbon isotope cycling calibrated and assessed against modern observational data[8-10], here adjusting only: atmospheric pCO_2 and $\delta^{13}C$, and ocean DIC, ALK, and Mg/Ca ratios, as described earlier[7,10].
3. Employing a representation of calcium carbonate ($CaCO_3$) production, preservation, and burial, that has been calibrated and assessed against modern observational data[11], and here adjusting only global weathering rates and the biological export $CaCO_3$:POC 'rain ratio' in the ocean, as described in references 17 and 19.

However, a number of areas of potential uncertainty remain (excepting ocean pH, which has been discussed in depth earlier):

- **Climate sensitivity**. The cGENIE model employs a fixed relationship between changes in CO_2 and radiative forcing, meaning that its climate sensitivity is effectively prescribed in our experiments. Paleogene climate sensitivity is potentially different from modern[12]. Our diagnosed change in atmosphere pCO_2 induces a global mean increase increase in ocean surface temperature across the PETM slightly lower than observations, allowing for climate sensitivity to be slightly higher than programmed into the model. Regardless, it is unlikely that Paleogene climate sensitivity uncertainty significantly impacts our findings as the contribution of climate-carbon cycle feedbacks are relatively small compared to emissions[13].
- **Surface climate**. The magnitude of surface ocean warming across the PETM simulated by cGENIE (2.3-6.0°C) is similar to recent proxy compilations (4-5°C)[14]. However, as compared to Mg/Ca and $\delta^{18}O$ reconstructed temperatures (Extended Data Fig. 8), ocean surface temperatures at the location of Site 401 in cGENIE are persistently about 7°C too low. Given that the magnitude of global mean warming is approximately correct, it is not obvious that the existence of a high Northern latitude cold bias leads to significant error in our deduced carbon emissions.
- **Ocean circulation**. Although cGENIE can reproduce observed gradients in benthic $\delta^{13}C$ and hence by inference, large scale ocean circulation patterns in the early Eocene[15], there is little constraint on the details of ocean circulation patterns and model-data misfits in the South Atlantic as revealed in our Site 1263 analysis reflecting substantial uncertainty here. However, because our inversion rests on surface seawater proxy data, uncertainty in (intermediate or deep) model circulation will be less critical to our conclusions.
- **Ocean geochemistry**. The assumed values for pre PETM ocean DIC and ALK, arise from assumptions regarding pCO_2 (itself constrained by matching observed deep ocean temperatures in the model) and the pattern of carbonate burial in the deep ocean (following ref. 17). Significant uncertainties exist on past ocean Mg/Ca ratios, which in turn influence the relationship between carbonate burial, DIC and ALK. However, radically different DIC inventories

(and hence isotopic buffering) are unlikely – a variety of previously published (and widely differing in methodology) analyses all produce a relatively consistent history of DIC, ALK, and surface ocean pH through the Cenozoic[7]. Furthermore, our initial pCO_2 assumption agrees with independent constraints[16].

- **Ocean productivity**. Both the initial state, and response across the PETM, is highly uncertain in both data and model. Changes in productivity not correctly accounted for in the model could impact the interpretation of both pH and $\delta^{13}C$, although given the relative uniformity of the surface ocean pH response, the greater potential for our conclusions to be affected would be in respect of $\delta^{13}C$. However, ocean surface $\delta^{13}C$ gradients (today) are much smaller than the total magnitude of the CIE lessening the impact that productivity uncertainty might have. Furthermore, we have already assumed and accounted for a significant uncertainty due to how the CIE is recorded and assimilated in the model.
- **The 'CCD' and carbonate buffering**. How well the deposition and preservation of $CaCO_3$ on the ocean floor is represented is arguably the most significant uncertainty. Although the model has been calibrated to an extensive paleo dataset[17], the $CaCO_3$:POC export ratio is assumed uniform and invariant. Errors in this would propagate through to errors (likely overestimates) in diagnosed carbon release[18], although we note that less buffered (and hence more sensitive to carbon release) models and associated scenarios, fail to fit observed pH proxy data[19].

Weathering and recovery feedbacks. Finally, the parameterizations of carbonate (F_{CaCO3}) and silicate (F_{CaSiO3}) weathering we assume are:

$$F_{CaCO_3} = F_{CaCO_3,0}\left(1 + k_{Ca}\,(T - T_0)\right)$$

$$F_{CaSiO_3} = F_{CaSiO_3,0}\, e^{\frac{1000E_a}{RT_0^2}(T-T_0)}$$

and are derived from references 15 and 20, respectively (see *Lord et al.*[21] for a complete description of terms plus discussion). These are both based solely on global mean surface land air temperature (T) and its deviation from a reference value (T_0). As such, we omit consideration of spatial patterns of temperature change, as well as runoff and plant productivity as potential modulating factors[22]. As an extreme test, in experiments with no weathering response to climate (Extended Data Table 1a), diagnosed cumulative carbon emissions are around 40% lower. A reasonable estimated uncertainty on our conclusions might then be half this: ±20% (±2000 PgC).

Overall, as might be expected for a protracted (>10 kyr total duration) geological event, the major model uncertainties likely lie in the long-term components and response of the global carbon cycle rather than details of ocean circulation or climate. Considerably more data (both spatially and temporary resolved, and for multiple proxies) and involved model-data analysis is needed for any more formal uncertainty to be placed on our model-derived PETM carbon release estimates beyond the sensitivity tests we have performed here.

References within Supplementary Information S1

1 Bornemann, A. *et al.* Persistent environmental change after the Paleocene-Eocene Thermal Maximum in the eastern North Atlantic. *Earth and Planetary Science Letters* **394**, 70-81 (2014).

2 Jennions, S. M., Thomas, E., Schmidt, D. N., Lunt, D. & Ridgwell, A. Changes in benthic ecosystems and ocean circulation in the Southeast Atlantic across Eocene Thermal Maximum 2. *Paleoceanography* **30**, 1059-1077 (2015).

3 Ridgwell, A. Interpreting transient carbonate compensation depth changes by marine sediment core modeling. *Paleoceanography* **22** (2007).

4 Zeebe, R. E. & Zachos, J. C. Reversed deep-sea carbonate ion basin gradient during Paleocene-Eocene thermal maximum. *Paleoceanography* **22**, Art. No.: PA3201 (2007).

5 Hargreaves, J. C., Annan, J. D., Edwards, N. R. & Marsh, R. An efficient climate forecasting method using an intermediate complexity Earth System Model and the ensemble Kalman filter. *Clim. Dyn.* **23**, 745-760 (2004).

6 Edwards, N. R. & Marsh, R. Uncertainties due to transport-parameter sensitivity in an efficient 3-D ocean-climate model. *Clim. Dyn.* **24**, 415-433 (2005).

7 Ridgwell, A. & Schmidt, D. N. Past constraints on the vulnerability of marine calcifiers to massive carbon dioxide release. *Nature Geoscience* **3**, 196-200 (2010).

8 Ridgwell, A. *et al.* Marine geochemical data assimilation in an efficient Earth System Model of global biogeochemical cycling. *Biogeosciences* **4**, 87-104 (2007).

9 Cao, L. *et al.* The role of ocean transport in the uptake of anthropogenic CO_2. *Biogeosciences* **6**, 375-390 (2009).

10 Turner, S. K. & Ridgwell, A. Development of a novel empirical framework for interpreting geological carbon isotope excursions, with implications for the rate of carbon injection across the PETM. *Earth and Planetary Science Letters* **435**, 1-13 (2016).

11 Ridgwell, A. & Hargreaves, J. C. Regulation of atmospheric CO_2 by deep-sea sediments in an Earth system model. *Glob. Biogeochem. Cycle* **21**, Art. No. GB2008 (2007).

12 Frieling, J. *et al.* Extreme warmth and heat-stressed plankton in the tropics during the Paleocene-Eocene Thermal Maximum. *Science Advances* **3** (2017).

13 Ridgwell, A., Zondervan, I., Hargreaves, J. C., Bijma, J. & Lenton, T. M. Assessing the potential long-term increase of oceanic fossil fuel CO_2 uptake due to CO_2-calcification feedback. *Biogeosciences* **4**, 481-492 (2007).

14 Dunkley Jones, T. *et al.* Climate model and proxy data constraints on ocean warming across the Paleocene-Eocene Thermal Maximum. *Earth-Science Reviews* **125**, 123-145 (2013).

15 Turner, S. K. & Ridgwell, A. Recovering the true size of an Eocene hyperthermal from the marine sedimentary record. *Paleoceanography* **28**, 700-712 (2013).

16 Schubert, B. A. & Jahren, A. H. Reconciliation of marine and terrestrial carbon isotope excursions based on changing atmospheric CO_2 levels. *Nature Communications* **4**, Art. No. 1653 (2013).

17 Panchuk, K., Ridgwell, A. & Kump, L. R. Sedimentary response to Paleocene-Eocene Thermal Maximum carbon release: A model-data comparison. *Geology* **36**, 315-318 (2008).

18 Zeebe, R. E., Zachos, J. C. & Dickens, G. R. Carbon dioxide forcing alone insufficient to explain Palaeocene-Eocene Thermal Maximum warming. *Nature Geoscience* **2**, 576-580 (2009).

19 Penman, D. E., Hönisch, B., Zeebe, R. E., Thomas, E. & Zachos, J. C. Rapid and sustained surface ocean acidification during the Paleocene-Eocene Thermal Maximum. *Paleoceanography* **29**, 357-369 (2014).

20 Brady, P. V. The Effect of Silicate Weathering on Global Temperature and Atmospheric CO_2. *J Geophys Res-Solid Earth* **96**, 18101-18106 (1991).

21 Lord, N. S., Ridgwell, A., Thorne, M. C. & Lunt, D. J. The 'long tail' of anthropogenic CO_2 decline in the atmosphere and its consequences for post-closure performance assessments for disposal of radioactive wastes. *Mineralogical Magazine* **79**, 1613-1623 (2015).

22 Colbourn, G., Ridgwell, A. & Lenton, T. M. The time scale of the silicate weathering negative feedback on atmospheric CO_2. *Glob. Biogeochem. Cycle* **29**, 583-596 (2015).

Supplementary Table S1. Foraminifera-based results and relative age model

DSDP Sample number	Depth (m)	Age relative to CIE (kyr) (following Röhl 2007)	Age relative to CIE (kyr) (following Farley & Eltgroth 2003)	$\delta^{11}B$ (‰)	2 S.D. (‰)	$\delta^{13}C$ (pdb) (‰)	$\delta^{18}O$ (pdb) (‰)	B/Ca µmol/mol	Mg/Ca mmol/mol	Al/Ca µmol/mol	mixed layer pH total scale	-2 SD	+2 SD
48-401-14R-1,4-6	198.55	504	533	14.15	0.34	3.56	-2.26	48	3.55	156	7.60	0.11	0.08
48-401-14R-1,30-32	198.81	475	499	14.14	0.29	3.98	-2.14	58	3.49	7	7.60	0.09	0.09
48-401-14R-1,45-47	198.96	459	480	14.00	0.34	4.32	-1.95	49	3.31	13	7.59	0.11	0.09
48-401-14R-1,91-93	199.42	408	419	14.38	0.34	4.38	-2.15	51	3.58	15	7.64	0.09	0.09
48-401-14R-1,110-113	199.62	386	394	13.85	0.31	4.29	-2.18	54	3.60	16	7.55	0.12	0.09
48-401-14R-1,120-122	199.71	375	381	14.07	0.46	4.09	-2.30	52	3.54	13	7.58	0.13	0.10
48-401-14R-1,138-140	199.89	355	358	14.67	0.27	4.10	-2.00	50	3.51	12	7.70	0.08	0.07
48-401-14R-2,8-10	200.09	333	331	14.59	0.27	4.30	-2.17	50	3.41	13	7.68	0.09	0.07
48-401-14R-2,31-33	200.32	308	301	14.83	0.30	4.07	-2.16	53	3.57	22	7.72	0.08	0.07
48-401-14R-2,50-52	200.51	287	276	14.64	0.28	4.46	-2.41	52	3.75	23	7.66	0.08	0.08
48-401-14R-2,72-74	200.73	262	248	14.36	0.33	4.13	-1.99	50	3.37	29	7.65	0.10	0.09
48-401-14R-2,91-93	200.92	241	223	14.54	0.30	4.38	-2.12	62	3.62	11	7.67	0.09	0.08
48-401-14R-2,110-112	201.11	220	198	14.09	0.30	4.03	-1.97	50	3.38	17	7.62	0.12	0.07
48-401-14R-2,129-131	201.30	199	173	14.67	0.37	4.03	-2.23	55	3.70	44	7.68	0.09	0.08
48-401-14R-2,148-150	201.49	178	148	14.05	0.57	3.76	-2.00	50	3.57	322	7.61	0.17	0.10
48-401-14R-3,11-13	201.62	163	131	14.09	0.22	3.03	-2.13	52	3.6	89	7.60	0.10	0.07
48-401-14R-3,16-18	201.67	157	124	13.65	0.39	3.85	-2.43	59	3.73	152	7.49	0.14	0.11
48-401-14R-3,21-23	201.72	150	118	14.67	0.30	3.29	-2.14	54	3.6	111	7.70	0.09	0.07
48-401-14R-3,26-27	201.77	138	114	14.29	0.82	3.23	-2.41	51	3.87	203	7.64	0.20	0.11
48-401-14R-3,37-39	201.88	121	109	14.44	0.45	3.34	-2.48	48	3.78	165	7.64	0.11	0.09
48-401-14R-3,47-49	201.98	107	104	14.34	0.31	3.21	-2.38	56	3.89	33	7.64	0.11	0.07
48-401-14R-3,58-60	202.09	90	97	14.37	0.37	3.59	-2.47	50	3.82	50	7.62	0.10	0.09
48-401-14R-3,68-70	202.19	76	90	14.37	0.30	2.93	-2.43	56	3.96	39	7.63	0.10	0.08
48-401-14R-3,74-76	202.25	68	84	14.43	0.21	2.62	-2.28	50	3.8	18	7.64	0.08	0.07
48-401-14R-3,79-81	202.30	61	80	13.77	0.47	3.27	-2.50	49	3.77	73	7.51	0.13	0.12
48-401-14R-3,84-86	202.35	55	76	14.66	0.25	2.59	-2.30	50	3.7	13	7.68	0.09	0.07
48-401-14R-3,90-92	202.41	47	70	13.71	0.73	3.18	-2.53	56	4.00	48	7.51	0.22	0.14
48-401-14R-3,96-98	202.47	17	28	13.22	0.48	1.02	-2.57	40	3.7	1442	7.38	0.20	0.14
48-401-14R-3,98-100	202.49	6	11	14.01	0.35	2.40	-2.37	63	3.9	3014	7.57	0.11	0.09
48-401-14R-3,101-104	202.53	-4	-7	13.67	0.35	3.43	-1.89	50	3.7	3398	7.52	0.13	0.11
48-401-14R-3, 103-105	202.55	-9	-18	14.92	0.40	4.43	-1.75	58	3.47	248	7.75	*n.a.*[*]	*n.a.*[*]
48-401-14R-3,112-114	202.63	-22	-44	14.91	0.75	4.46	-1.69	54	3.34	527	7.75	0.14	0.11
48-401-14R-3,122-123	202.73	-41	-71	14.33	0.37	4.11	-1.39	52	3.32	480	7.68	0.10	0.09
48-401-14R-3,133-134	202.84	-63	-102	14.74	0.38	4.53	-1.59	58	3.41	280	7.74	0.10	0.07
48-401-14R-3,143-145	202.94	-80	-131	14.90	0.36	4.36	-1.63	56	3.43	234	7.75	0.08	0.08
48-401-14R-4, 22-23	203.23	-126	-212	14.66	0.41	4.10	-1.20	54	3.47	91	7.75	0.10	0.08
48-401-14R-4, 32-33	203.33	-142	-240	14.21	0.34	3.94	-1.18	49	3.44	247	7.68	0.11	0.08
48-401-14R-4, 39-40	203.40	-154	-260	14.95	0.33	4.31	-1.22	57	3.46	435	7.79	0.09	0.07
48-401-14R-4, 70-71	203.71	-204	-347	14.44	0.39	4.46	-1.15	48	3.32	207	7.72	0.11	0.08
48-401-14R-4, 90-91	203.91	-237	-403	14.92	0.43	4.20	-1.02	44	3.46	340	7.79	0.09	0.08
48-401-14R-5, 64-66	205.15	-439	-754	15.63	0.61	4.36	-1.14	43	3.58	90	7.89	0.11	0.08

[*] *Note that no error is associated with this depth since this level is used to tie d11B based pH estimates to GENIE ESM (see methods)*

CIE = Carbon Isotope Excursion (see main publication for more information)

Supplementary Table S2. Bulk carbonate stable isotope compositions

DSDP Leg/Exp	Site	Core	Type	Section	Half (A/W)	Interval (cm) Top	Interval (cm) Bottom	Composite Depth (m)	Age relative to CIE (kyr) (following Röhl 2007)	Age relative to CIE (kyr) (following Farley & Eltgroth 2003)	$\delta^{13}C$ (pdb) (‰)	$\delta^{18}O$ (pdb) (‰)
48	401	14	R	2	A	100	101	201.01	232	211	1.47	-1.09
48	401	14	R	2	A	101	102	201.02	230	210	1.65	-0.92
48	401	14	R	2	A	102	103	201.03	229	209	1.74	-0.89
48	401	14	R	2	A	103	104	201.04	228	208	1.72	-0.97
48	401	14	R	2	A	104	105	201.05	227	206	1.74	-0.91
48	401	14	R	2	A	105	106	201.06	226	205	1.76	-0.82
48	401	14	R	2	A	106	107	201.07	225	204	1.49	-0.85
48	401	14	R	2	A	107	108	201.08	224	202	1.73	-1.06
48	401	14	R	2	A	108	109	201.09	223	201	1.74	-0.98
48	401	14	R	2	A	109	110	201.10	222	200	1.67	-0.89
48	401	14	R	2	A	110	111	201.11	220	198	1.78	-1.01
48	401	14	R	2	A	111	112	201.12	219	197	1.73	-0.92
48	401	14	R	2	A	112	113	201.13	218	196	1.71	-1.04
48	401	14	R	2	A	113	114	201.14	217	194	1.73	-0.87
48	401	14	R	2	A	114	115	201.15	216	193	1.53	-0.89
48	401	14	R	2	A	115	116	201.16	215	192	1.75	-0.82
48	401	14	R	2	A	116	117	201.17	214	191	1.70	-0.81
48	401	14	R	2	A	117	118	201.18	213	189	1.69	-0.83
48	401	14	R	2	A	118	119	201.19	212	188	1.96	-1.16
48	401	14	R	2	A	119	120	201.20	210	187	1.71	-0.94
48	401	14	R	2	A	120	121	201.21	209	185	1.76	-0.77
48	401	14	R	2	A	121	122	201.22	208	184	1.80	-0.80
48	401	14	R	2	A	122	123	201.23	207	183	1.79	-0.80
48	401	14	R	2	A	123	124	201.24	206	181	1.76	-0.65
48	401	14	R	2	A	124	125	201.25	205	180	1.81	-0.78
48	401	14	R	2	A	125	126	201.26	204	179	1.78	-0.97
48	401	14	R	2	A	127	128	201.28	201	176	1.68	-0.96
48	401	14	R	2	A	128	129	201.29	200	175	1.65	-1.03
48	401	14	R	2	A	129	130	201.30	199	173	1.73	-1.04
48	401	14	R	2	A	130	131	201.31	198	172	1.68	-0.90
48	401	14	R	2	A	131	132	201.32	197	171	1.65	-0.92
48	401	14	R	2	A	132	133	201.33	196	170	1.65	-0.82
48	401	14	R	2	A	133	134	201.34	195	168	1.64	-0.92
48	401	14	R	2	A	134	135	201.35	194	167	1.61	-0.93
48	401	14	R	2	A	135	136	201.36	193	166	1.66	-0.91
48	401	14	R	2	A	136	137	201.37	191	164	1.65	-0.91
48	401	14	R	2	A	137	138	201.38	190	163	1.53	-0.79
48	401	14	R	2	A	138	139	201.39	189	162	1.61	-0.93
48	401	14	R	2	A	139	140	201.40	188	160	1.59	-0.85
48	401	14	R	2	A	140	141	201.41	187	159	1.44	-0.90
48	401	14	R	2	A	141	142	201.42	186	158	1.51	-0.83
48	401	14	R	2	A	142	143	201.43	185	156	1.46	-0.90
48	401	14	R	2	A	143	144	201.44	184	155	1.38	-0.90
48	401	14	R	2	A	144	145	201.45	183	154	1.47	-0.83
48	401	14	R	2	A	145	146	201.46	181	153	1.45	-0.92
48	401	14	R	2	A	146	147	201.47	180	151	1.53	-0.89
48	401	14	R	2	A	147	148	201.48	179	150	1.43	-0.92
48	401	14	R	2	A	148	149	201.49	178	149	1.51	-0.94
48	401	14	R	2	A	149	150	201.50	177	147	1.64	-1.01
48	401	14	R	3	A	1	2	201.52	175	145	1.52	-0.73
48	401	14	R	3	A	2	3	201.53	174	143	1.50	-0.79
48	401	14	R	3	A	3	4	201.54	173	142	1.43	-0.87
48	401	14	R	3	A	4	5	201.55	171	141	1.56	-0.74
48	401	14	R	3	A	5	6	201.56	170	139	1.38	-0.69
48	401	14	R	3	A	6	7	201.57	169	138	1.53	-0.89
48	401	14	R	3	A	7	8	201.58	168	137	1.46	-0.92
48	401	14	R	3	A	8	9	201.59	167	135	1.52	-0.88
48	401	14	R	3	A	9	10	201.60	166	134	1.48	-1.02
48	401	14	R	3	A	10	11	201.61	165	133	1.47	-1.05
48	401	14	R	3	A	11	12	201.62	164	132	1.38	-1.03
48	401	14	R	3	A	12	13	201.63	162	130	1.50	-0.80
48	401	14	R	3	A	13	14	201.64	161	129	1.49	-0.94
48	401	14	R	3	A	14	15	201.65	160	128	1.50	-0.88
48	401	14	R	3	A	15	16	201.66	159	126	1.54	-0.82
48	401	14	R	3	A	16	17	201.67	158	125	1.41	-1.26
48	401	14	R	3	A	17	18	201.68	157	124	1.42	-1.27
48	401	14	R	3	A	18	19	201.69	155	122	1.42	-1.21
48	401	14	R	3	A	19	20	201.70	154	121	1.25	-1.16
48	401	14	R	3	A	20	21	201.71	153	120	1.37	-1.00
48	401	14	R	3	A	21	22	201.72	151	118	1.38	-0.98
48	401	14	R	3	A	22	23	201.73	149	117	1.36	-1.03
48	401	14	R	3	A	23	24	201.74	146	116	1.31	-1.06
48	401	14	R	3	A	24	25	201.75	143	115	1.41	-1.17
48	401	14	R	3	A	25	26	201.76	141	115	1.41	-1.11
48	401	14	R	3	A	26	27	201.77	138	114	1.33	-1.06
48	401	14	R	3	A	27	28	201.78	136	113	1.16	-0.99
48	401	14	R	3	A	28	29	201.79	135	113	1.12	-0.94
48	401	14	R	3	A	29	30	201.80	133	112	1.17	-1.02
48	401	14	R	3	A	30	31	201.81	132	112	1.21	-0.96
48	401	14	R	3	A	31	32	201.82	130	111	1.14	-0.92
48	401	14	R	3	A	32	33	201.83	129	111	1.17	-0.99
48	401	14	R	3	A	33	34	201.84	128	111	1.17	-0.94
48	401	14	R	3	A	34	35	201.85	126	110	1.22	-0.94

48	401	14	R	3	A	35	36	201.86	125	110	1.12	-0.90
48	401	14	R	3	A	36	37	201.87	123	109	1.13	-1.00
48	401	14	R	3	A	37	38	201.88	122	109	1.18	-0.94
48	401	14	R	3	A	38	39	201.89	120	108	1.21	-0.91
48	401	14	R	3	A	39	40	201.90	119	108	1.17	-0.89
48	401	14	R	3	A	40	41	201.91	118	107	1.13	-0.94
48	401	14	R	3	A	41	42	201.92	116	107	1.17	-0.93
48	401	14	R	3	A	42	43	201.93	115	107	1.13	-0.98
48	401	14	R	3	A	43	44	201.94	113	106	1.12	-0.94
48	401	14	R	3	A	44	45	201.95	112	106	1.16	-0.87
48	401	14	R	3	A	45	46	201.96	110	105	1.14	-0.86
48	401	14	R	3	A	46	47	201.97	109	105	1.19	-0.94
48	401	14	R	3	A	47	48	201.98	107	104	1.17	-0.89
48	401	14	R	3	A	48	49	201.99	106	104	1.15	-0.91
48	401	14	R	3	A	49	50	202.00	104	103	1.19	-0.95
48	401	14	R	3	A	50	51	202.01	103	103	1.19	-0.99
48	401	14	R	3	A	51	52	202.02	101	102	1.17	-0.93
48	401	14	R	3	A	52	53	202.03	100	101	1.18	-0.91
48	401	14	R	3	A	53	54	202.04	98	101	1.20	-0.82
48	401	14	R	3	A	54	55	202.05	97	100	1.17	-0.95
48	401	14	R	3	A	55	56	202.06	95	100	1.15	-0.90
48	401	14	R	3	A	56	57	202.07	94	99	1.22	-0.93
48	401	14	R	3	A	57	58	202.08	92	98	0.87	-0.88
48	401	14	R	3	A	58	59	202.09	91	98	1.14	-0.92
48	401	14	R	3	A	59	60	202.10	89	97	1.16	-0.85
48	401	14	R	3	A	60	61	202.11	88	96	1.16	-0.91
48	401	14	R	3	A	61	62	202.12	86	95	1.18	-0.87
48	401	14	R	3	A	62	63	202.13	85	95	1.14	-0.92
48	401	14	R	3	A	63	64	202.14	84	94	1.18	-0.81
48	401	14	R	3	A	64	65	202.15	82	93	1.04	-1.00
48	401	14	R	3	A	65	66	202.16	81	92	1.06	-1.04
48	401	14	R	3	A	66	67	202.17	79	92	1.14	-0.96
48	401	14	R	3	A	67	68	202.18	78	91	1.12	-1.05
48	401	14	R	3	A	68	69	202.19	76	90	1.12	-0.97
48	401	14	R	3	A	69	70	202.20	75	89	1.10	-1.05
48	401	14	R	3	A	70	71	202.21	74	88	1.17	-0.97
48	401	14	R	3	A	71	72	202.22	72	88	1.14	-0.91
48	401	14	R	3	A	72	73	202.23	71	87	1.11	-1.01
48	401	14	R	3	A	73	74	202.24	70	86	1.14	-0.99
48	401	14	R	3	A	74	75	202.25	68	85	1.15	-1.14
48	401	14	R	3	A	75	76	202.26	67	84	1.06	-0.97
48	401	14	R	3	A	76	77	202.27	66	83	1.12	-0.98
48	401	14	R	3	A	77	78	202.28	65	82	1.14	-1.04
48	401	14	R	3	A	78	79	202.29	63	81	1.11	-0.93
48	401	14	R	3	A	79	80	202.30	62	80	1.11	-1.04
48	401	14	R	3	A	80	81	202.31	61	80	1.11	-0.91
48	401	14	R	3	A	81	82	202.32	59	79	1.07	-1.04
48	401	14	R	3	A	82	83	202.33	58	78	1.11	-1.06
48	401	14	R	3	A	83	84	202.34	57	77	1.08	-0.92
48	401	14	R	3	A	84	85	202.35	55	76	1.00	-1.03
48	401	14	R	3	A	85	86	202.36	54	75	1.10	-1.04
48	401	14	R	3	A	86	87	202.37	53	74	1.10	-1.04
48	401	14	R	3	A	87	88	202.38	51	73	1.09	-1.04
48	401	14	R	3	A	88	89	202.39	50	73	1.12	-1.01
48	401	14	R	3	A	89	90	202.40	49	72	1.13	-1.10
48	401	14	R	3	A	90	91	202.41	47	71	1.11	-1.03
48	401	14	R	3	A	91	92	202.42	44	67	0.72	-1.44
48	401	14	R	3	A	92	93	202.43	39	60	0.69	-1.36
48	401	14	R	3	A	93	94	202.44	34	53	0.77	-1.17
48	401	14	R	3	A	94	95	202.45	29	46	0.78	-1.16
48	401	14	R	3	A	95	96	202.46	24	39	0.64	-1.10
48	401	14	R	3	A	96	97	202.47	19	32	0.73	-1.15
48	401	14	R	3	A	97	98	202.48	14	24	0.03	-1.59
48	401	14	R	3	A	98	99	202.49	9	15	1.41	-1.11
48	401	14	R	3	A	99	100	202.50	5	8	2.25	-0.89
48	401	14	R	3	A	100	101	202.51	2	3	1.83	-1.19
48	401	14	R	3	A	101	102	202.52	-1	-2	2.31	-0.70
48	401	14	R	3	A	102	103	202.53	-4	-7	2.28	-0.51
48	401	14	R	3	A	103	104	202.54	-6	-12	2.07	-0.69
48	401	14	R	3	A	104	105	202.55	-9	-18	2.17	-0.55
48	401	14	R	3	A	105	106	202.56	-10	-21	2.13	-0.66
48	401	14	R	3	A	106	107	202.57	-12	-24	2.07	-0.64
48	401	14	R	3	A	107	108	202.58	-13	-27	2.13	-0.62
48	401	14	R	3	A	108	109	202.59	-15	-30	1.93	-0.63
48	401	14	R	3	A	109	110	202.60	-16	-33	1.97	-0.51
48	401	14	R	3	A	110	111	202.61	-18	-36	1.89	-0.64
48	401	14	R	3	A	111	112	202.62	-19	-39	2.00	-0.60
48	401	14	R	3	A	112	113	202.63	-21	-42	1.99	-0.57
48	401	14	R	3	A	113	114	202.64	-23	-45	1.95	-0.64
48	401	14	R	3	A	114	115	202.65	-25	-48	1.99	-0.60
48	401	14	R	3	A	115	116	202.66	-27	-51	2.17	-0.61
48	401	14	R	3	A	116	117	202.67	-29	-54	1.96	-0.68
48	401	14	R	3	A	117	118	202.68	-31	-57	2.10	-0.66
48	401	14	R	3	A	118	119	202.69	-33	-59	2.13	-0.58
48	401	14	R	3	A	119	120	202.70	-35	-62	2.18	-0.60
48	401	14	R	3	A	120	121	202.71	-37	-65	2.24	-0.54
48	401	14	R	3	A	121	122	202.72	-39	-68	2.20	-0.57

48	401	14	R	3	A	122	123	202.73	-41	-71	2.24	-0.52
48	401	14	R	3	A	123	124	202.74	-43	-73	2.31	-0.51
48	401	14	R	3	A	124	125	202.75	-45	-76	2.26	-0.52
48	401	14	R	3	A	125	126	202.76	-47	-79	2.29	-0.56
48	401	14	R	3	A	126	127	202.77	-49	-82	2.27	-0.53
48	401	14	R	3	A	127	128	202.78	-51	-85	2.30	-0.61
48	401	14	R	3	A	128	129	202.79	-53	-88	2.22	-0.54
48	401	14	R	3	A	129	130	202.80	-55	-90	2.10	-0.18
48	401	14	R	3	A	130	131	202.81	-57	-93	2.28	-0.51
48	401	14	R	3	A	131	132	202.82	-59	-96	2.25	-0.50
48	401	14	R	3	A	132	133	202.83	-61	-99	2.26	-0.60
48	401	14	R	3	A	133	134	202.84	-63	-102	2.24	-0.42
48	401	14	R	3	A	134	135	202.85	-64	-104	2.25	-0.60
48	401	14	R	3	A	135	136	202.86	-66	-107	2.24	-0.51
48	401	14	R	3	A	136	137	202.87	-68	-110	2.24	-0.45
48	401	14	R	3	A	137	138	202.88	-69	-113	2.28	-0.57
48	401	14	R	3	A	138	139	202.89	-71	-116	2.26	-0.51
48	401	14	R	3	A	139	140	202.90	-73	-119	2.31	-0.61
48	401	14	R	3	A	140	141	202.91	-74	-121	2.22	-0.55
48	401	14	R	3	A	141	142	202.92	-76	-124	2.27	-0.56
48	401	14	R	3	A	142	143	202.93	-77	-127	2.27	-0.65
48	401	14	R	3	A	143	144	202.94	-79	-130	2.26	-0.58
48	401	14	R	3	A	144	145	202.95	-81	-133	2.28	-0.64
48	401	14	R	3	A	145	146	202.96	-82	-135	2.33	-0.58
48	401	14	R	3	A	146	147	202.97	-84	-138	2.28	-0.53
48	401	14	R	3	A	147	148	202.98	-86	-141	2.30	-0.50
48	401	14	R	3	A	148	149	202.99	-87	-144	2.34	-0.53
48	401	14	R	3	A	149	150	203.00	-89	-147	2.26	-0.50
48	401	14	R	4	A	5	6	203.06	-99	-164	2.26	-0.39
48	401	14	R	4	A	10	11	203.11	-107	-178	2.23	-0.39
48	401	14	R	4	A	15	16	203.16	-115	-192	2.23	-0.43
48	401	14	R	4	A	20	21	203.21	-123	-206	2.12	-0.40
48	401	14	R	4	A	25	26	203.26	-131	-220	2.11	-0.40
48	401	14	R	4	A	30	31	203.31	-139	-234	2.21	-0.59
48	401	14	R	4	A	35	36	203.36	-147	-248	2.33	-0.47
48	401	14	R	4	A	40	41	203.41	-155	-262	2.26	-0.39
48	401	14	R	4	A	45	46	203.46	-164	-276	2.48	-0.41
48	401	14	R	4	A	50	51	203.51	-172	-291	2.45	-0.34
48	401	14	R	4	A	55	56	203.56	-180	-305	2.40	-0.16
48	401	14	R	4	A	60	61	203.61	-188	-319	2.43	-0.20
48	401	14	R	4	A	65	66	203.66	-196	-333	2.49	-0.19
48	401	14	R	4	A	70	71	203.71	-204	-347	2.56	-0.26
48	401	14	R	4	A	75	76	203.76	-212	-361	2.55	-0.29
48	401	14	R	4	A	80	81	203.81	-220	-375	2.58	-0.33
48	401	14	R	4	A	85	86	203.86	-229	-389	2.52	-0.20
48	401	14	R	4	A	90	91	203.91	-237	-403	2.48	-0.24
48	401	14	R	4	A	95	96	203.96	-245	-417	2.49	-0.41
48	401	14	R	4	A	100	101	204.01	-253	-432	2.57	-0.38
48	401	14	R	4	A	105	106	204.06	-261	-446	2.56	-0.22
48	401	14	R	4	A	110	111	204.11	-269	-460	2.61	-0.21
48	401	14	R	4	A	115	116	204.16	-277	-474	2.56	-0.12
48	401	14	R	4	A	120	121	204.21	-285	-488	2.57	-0.20
48	401	14	R	4	A	125	126	204.26	-293	-502	2.44	-0.09
48	401	14	R	4	A	130	131	204.31	-302	-516	2.37	-0.24
48	401	14	R	4	A	135	136	204.36	-310	-530	2.33	-0.37
48	401	14	R	4	A	140	141	204.41	-318	-544	2.56	-0.35
48	401	14	R	4	A	145	146	204.46	-326	-558	2.50	-0.15